Department of Precision and Microsystems Engineering

Fabrication of nanodiamond loaded photoresist microstructures using two-photon polymerization

Halis Tuztasi

Report no : 2021.056
Coach : Dr. J.G. Buijnsters
Professor : Dr. J.G. Buijnsters
Specialisation : Micro and Nano Engineering
Type of report : Master Thesis
Date : 13-08-2021

Fabrication of nanodiamond loaded photoresist microstructures using two-photon polymerization

by

Halis Tuztasi

to obtain the degree of Master of Science in Mechanical Engineering
at the Delft University of Technology,
to be defended publicly on Friday August 27, 2021 at 14:00 PM.

Student number:	4324234	
Project duration:	October 1, 2019 – August 27, 2021	
Thesis committee:	Dr. J.G. Buijnsters,	TU Delft, Supervisor
	Dr. A. Accardo,	TU Delft
	Dr. D. Fan,	TU Delft

This thesis is confidential and cannot be made public until September 1, 2023.

TU Delft

Preface

I would like to start by thanking my supervisor Ivan Buijnsters for his support and guidance throughout the project. Furthermore, I want to thank Angelo Accardo and Daniel Fan for being part of my defense committee. In particular, I would like to acknowledge the daily support I received from Ahmed Sharaf, even though he was not directly involved in my project. Furthermore, I would like to thank Tomas Manzaneque Garcia and Runze Wang (Reactor Institute Delft) for their help with the fluorescence microscopy and dynamic light scattering experiments. Lastly, I would like to thank the NanoScribe master student team (Qais, Damla, Jikke, Nastaran and Pieter) for the fun times in and around the labs.

Halis Tuztasi
Delft, August 2021

Abstract

Diamond is known for its outstanding material properties, including highest hardness, excellent chemical resistance and high thermal conductivity. Diamond, which is normally formed in high pressure and temperature environments, can also be produced as polycrystalline thin films in reduced pressure environments through chemical vapor deposition (CVD). Microfabricated diamond microstructures find their applications in a variety of micro-devices and sensors exploiting diamond's physical and chemical properties.

Current diamond microfabrication methods are limited to simple 2D and 2.5D structures, and rely on costly processes to pattern the diamond films after their growth. At present, a method to produce arbitrary 3D diamond microstructures is not available, thereby limiting the exploitation of microstructured diamond . Therefore, a novel bottom-up approach to produce diamond loaded microstructures using the principle of two-photon polymerization (2PP) was explored in this MSc thesis project.

The diamond loaded microstructures were developed through a monodispersed nanodiamond loaded photoresist (1 weight percentage), produced by mixing photoresist SU-8 2075 with an acetone based nanofluid containing diamond nanoparticles ranging from 3.5 to 6.0 nm in size. Using the loaded resin, the 2PP process was optimized for micropillar arrays of 20 microns in diameter and height. As a result, by utilizing the optimized parameters, microstructures with features of 2 microns and aspect ratios of 1:5 were obtained. Furthermore, the loaded microstructures showed to have a Young's modulus of 3.2 ± 0.22 GPa compared to 2.4 ± 0.10 GPa for the base resin, thus exhibiting an increase of 33%.

The obtained diamond loaded microstructures are expected to form a base for future pyrolysis and CVD processes, thereby enabling the fabrication of complex 3D diamond coated glassy carbon core-shell microstructures. These microstructures with high surface-to-volume ratios might solve the largest bottleneck in the advance of hierarchical boron-doped diamond microelectrodes for various electrochemical applications.

Contents

List of Abbreviations

2PP	Two-photon polymerization
BDD	Boron-doped diamond
C-MEMS	Carbon microelectromechanical systems
CVD	Chemical vapor deposition
DLS	Dynamic light scattering
HFCVD	Hot filament chemical vapor deposition
HPHT	High-pressure high-temperature
IPA	Isopropyl alcohol
MAPTMS	3 (trimethoxysilyl) propyl methacrylate
MCD	Microcrystalline diamond
MEMS	Microelectromechanical systems
NCD	Nanocrystalline diamond
NDs	Nanodiamonds
NPs	Nanoparticles
PAGs	Photoacid generators
PDMS	Polydimethylsiloxane
PGMEA	1-methoxy-2-propanol acetate
PME	Precision and Microsystems Engineering
PR	Photoresist
SEM	Scanning electronmicroscopy
TEM	Transmission electron microscopy
TNW	Faculty of applied sciences
Wt.%	Weight percentage

1 Introduction

In the vastly emerging fields of Microelectromechanical systems (MEMS), microfluidics and sensors, an effort is made to find alternatives to gap the mechanical and chemical limitations of the broadly used silicon [1, 2]. One promising material for this purpose is diamond. Diamond is known for its outstanding physical, chemical and electrical properties where it is often positioned at the extremes, owing to diamond's high hardness (60-100 GPa) [3], high Young's modulus (∼1000 GPa) [3] and high thermal conductivity (∼2200 W/mK) [4]. These material properties allow diamond-based components and devices to find far-ranging applications, for example, in electrochemistry as electrodes for wastewater treatment [5, 6], in telecommunications as heat spreaders [7], and in (bio)chemical sensing optionally in combination with surface functionalization [8, 9].

For the use of diamond in MEMS, microfluidics, and sensors, diamond films are mainly lab grown with a variety of chemical vapor deposition (CVD) processes. To functionalize the material for its application, patterning the diamond films to a variety of micrometer sized shapes, ranging from pillars to free standing beams, is essential. This microfabrication of diamond structures can be divided into two main groups of top-down (a) and bottom-up (b) microfabrication, as shown in Figure 1.1. With top-down microfabrication, the complete substrate surface is first seeded with nanoparticles (NPs) by using spin coating, dip coating or drop casting [10]. After this seeding step, polycrystalline diamond is grown with CVD and patterned by removing excess diamond from the bulk material film with traditional lithography. Patterning the diamond films include the use of processes such as reactive ion etching and ion beam milling [10, 11, 12]. With regards to the bottom-up microfabrication, NPs are directly patterned before CVD with selective seeding and grown only on the desired areas, which contrasts with the costly and complex top-down approach. Methods of selective seeding include template assisted CVD [13], inkjet printing [8] and traditional lithography with photoresists which are either used as masks [14, 15] or loaded with diamond NPs [16, 17]. The latter method of patterning diamond microstructures with photoresist is an attractive method as a broad variety of patterning options are available from traditional lithography or multiphoton lithography, such as two-photon polymerization (2PP). The use of loaded photoresist to directly pattern 2D diamond films has already been demonstrated [16, 17], however, no effort has been made to pattern and grow 3D diamond loaded microstructures as these resins deteriorate after exposure to the harsh CVD environment. One way to improve the resistance of these photoresists is by the use of pyrolysis [18]. Pyrolysis is proved to positively alter the physical and chemical resistance of 2PP resins by carbonizing the polymers in a heated and inert environment, increasing the chance of survival during CVD. Examples of the pyrolysis of particle loaded resins include the use of metal particles such as nickel [19], zinc [20] and iron [21].

Considering the available diamond microfabrication processes, both top-down and bottom-up microfabrication methods are currently limited to simple 2D and 2.5D structures. Top-down microfabrication methods demand the use of costly processes to pattern the diamond structures after CVD [10, 11, 12]. The bottom-up approach is beneficial in terms of cost-effectiveness [8] as the etching process is eliminated but does not add significant improvement in terms of design freedom. One promising approach to bridge the gap to the fabrication of complex 3D diamond microstructures is by combining the use of diamond loaded photoresists with 2PP. Therefore, the aim of this study is the production of 3D microstructures composed of diamond NP loaded photoresist. This production process is expected to form a base for future pyrolysis and CVD.

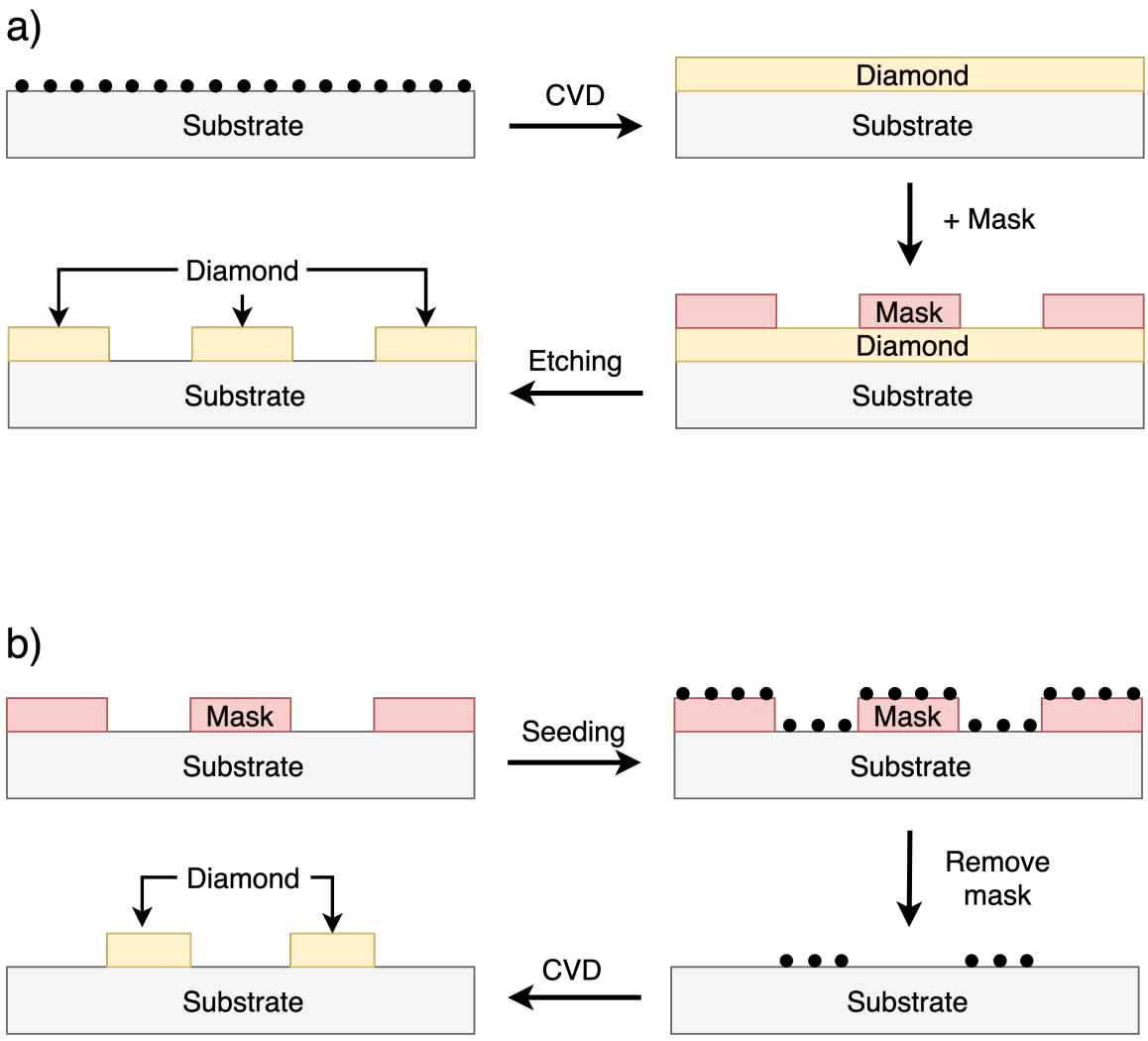

Figure 1.1: Schematic views of the top-down (a) and bottom-up (b) diamond microfabrication methods.

To provide a background to the envisaged production process of 3D diamond microstructures, Chapter 2 reviews the state-of-the-art on the synthesis of diamond and diamond NPs. Furthermore, the working principles of 2PP are elaborated and some potential future applications of the diamond loaded microstructures are given. This will be followed by a brief description of the knowledge gap and the research questions in Chapter 3. Then, the project plan is defined in Chapter 4 and split into different project steps. The individual project steps are elaborated in Chapter 5 where the used materials and methods are described. Following, the results are discussed in Chapter 6 and the conclusions are given in Chapter 7. Lastly, Chapter 8 elaborates on recommendations for future research.

2

Theoretical background

The dispersion behavior of diamond particles in polymer resins needs to be researched to successfully develop a micropatterning method for diamond NPs loaded photoresist resins. In this chapter, the state-of-the-art of synthetic diamond is briefly reviewed. This is followed by highlighting of the origin of diamond NPs and their behavior in suspensions and composites. Then, details are given about the basic working principles of 2PP processes, and the chapter concludes with a brief discussion of potential applications of diamond-loaded polymers and microstructures.

2.1. Synthetic diamond

Diamond is naturally formed in the earth's crust under high pressure and high temperature environments. By mimicking these natural growth conditions, diamond can be formed synthetically with high-pressure high-temperature (HPHT) synthesis [20]. The HPHT process typically creates single crystal diamonds, with sizes ranging up to a few millimeters. Another method to synthesize diamond is the CVD process. During the CVD process, single-crystal diamond or polycrystalline diamond films are grown at reduced pressure and at elevated temperature. The diamond is grown with the use of hydrogen and carbon containing gasses like methane. Adding other molecules to the gas mixture during the process makes elemental doping of the diamond possible. Elemental doping (e.g., B, P) enables the possibility to tune the newly grown diamonds' physical and chemical properties to satisfy the applications needs. With CVD, thin films can be grown on either diamond or non-diamond substrates, including metals (e.g., W, Nb), semiconductors (e.g., Si) and oxides (e.g., SiO2). For non-diamond substrates, pretreatment in the form of seeding with diamond nanoparticles is necessary. These diamond particles act as nucleation points on the substrate surface, thereby initiating the growth of diamond locally. Finally, extended growth of these diamond particles by CVD results in the formation of uniform diamond films throughout the substrate plane [22]. Depending on the process parameters (e.g., pressure, gas flow, substrate temperature and growth time), average grain sizes range from several hundreds of nanometers to several micrometers throughout the deposited CVD diamond film [2]. Scanning electron microscopy (SEM) images of typical CVD diamond film materials are shown in Figure 2.1.

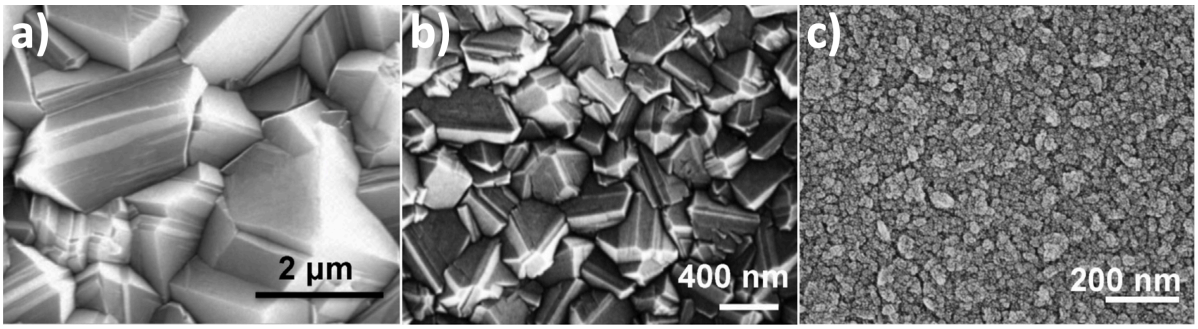

Figure 2.1: SEM images of microcrystalline diamond (MCD) and nanocrystalline diamond (NCD) films (middle and right) grown by CVD, Note the decreasing average crystallite size from left to right, respectively. [23]

2.2. Diamond nanoparticles

Diamond NPs, or nanodiamonds (NDs), can be produced by crushing CVD and HPHT diamond, and by detonation and pulsed laser ablation processes [20]. Diamond NPs obtained from crushing CVD diamond are typically well faceted and vary broadly in shape (Fig. 2.2a) [24]. These particles sizes also vary strongly in size, typically between several tens of nm to sub-10 nm. NDs produced by detonation (Figure 2.2b), on the other hand, show a narrow size distribution with average diameter of 5 nm [25] and generally consist of a core of sp^3 type carbon (i.e., diamond matrix) and a shell of sp^2-hybridized carbon to stabilize and terminate the surface. Diamond NPs produced by laser ablation generally consist of a core of sp^3 type carbon and a shell of sp^2-hybridized carbon, similar to NDs produced by detonation processes [26]. Dependent on the process parameters, the average sizes of NDs produced by laser ablation can vary from 4-5 nm to several hundreds of nm [27].

The surface termination has a large impact on the physical and chemical properties of the various types of diamond NPs [28] . The solubility and structure are greatly defined by the outer surface. By functionalizing the surface, for example with amine derivatives, their solubility in different hydrophobic organic solvents can be improved, such as in benzene and toluene. By adding surfactants to the diamond NPs, the stability of dispersions inside different solvents together with their zeta potential can be modified [29]. The increased solubility and stability caused by altering the surface makes it possible to incorporate stable dispersions of diamond NPs in polymers to produce diamond-polymer composites [28].

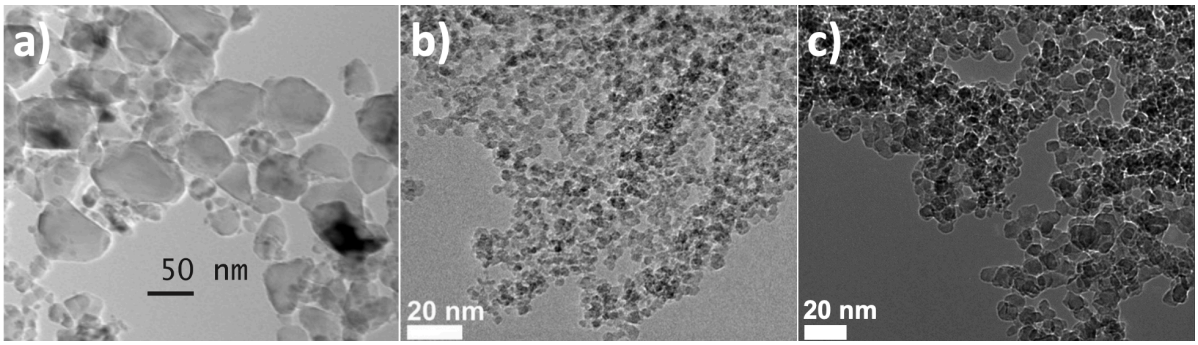

Figure 2.2: Transmission electron microscopy (TEM) images of diamond nanoparticles produced by crushing CVD diamond [30], detonation [25] and pulsed laser ablation [27], respectively.

2.3. Diamond-polymer composites

Diamond's mechanical and thermal properties make diamond-polymer composites a good candidate for the engineering of advanced multifunctional materials [31]. The successful incorporation of NDs into polymers can lead to composites with improved mechanical and thermal properties as compared to bare polymer material. The addition of even small amounts of NDs to epoxy resins (i.e., less than 1 weight percentage), for example, may improve the ultimate tensile strength and Young's modulus of these resins [32]. Moreover, improvements on the tensile strength were also seen on silicon rubber-based ND composites, compared to its respective neat polymer [33]. The same study also noted improvements on the thermal conductivity of these silicon rubber-ND composites. Furthermore, improvements in the heat resistance, such as the glass transition and thermal degradation temperatures, were observed for Poly methyl methacrylate based ND composites [34]. The improvement of the physical and chemical properties of ND-polymer suspensions are greatly impacted by the dispersion of the diamond NPs [35]. Agglomerates influence the coherence between the NPs and the polymer, often resulting in composites with even poorer properties compared to the base polymer.

For the preparation of these ND-polymer composites and other ND containing suspensions, a frequently used process is ultrasonic disruption [36]. With sonication, cavitation is induced inside the target material by sound waves to monodisperse the NPs inside the liquid. Dispersing the NPs can either be done with direct or indirect sonication. With regards to direct sonication, the sonication probe is inserted in the material and produces the waves directly inside the material. Considering indirect sonication, the sample is placed in a liquid bath and the ultrasonic waves are transferred through the bath to the

target. Typically, direct sonication provides local highly concentrated power around the probe whereas indirect sonication yields more homogeneous sonication with lower power density throughout the material. Owing to the increased power input, direct sonication is preferred over indirect sonication for the process of suspending dry powders.

2.4. Two-photon polymerization

An interesting application field for diamond-polymer composites are photoresists, as these composite materials with altered properties can be patterned with photolithography [16, 17]. One appealing approach is the use of 2PP, which is a maskless patterning method in the family of multiphoton photolithography processes. During the 2PP process, photosensitive polymers are locally polymerized by using a focused laser beam. At the focal point of the laser (voxel), the laser energy exceeds the polymerization threshold of the material and alters its structure and material properties. This laser induced energy can be expressed in terms of exposure, build up by the amount of laser power and the travel speed of the laser inside the material (scan speed). Depending on the type of photoresist, the laser exposed areas degrade (positive tone photoresist) or crosslink (negative tone photoresist) after exposure. Due to changes in chemical resistance at the laser treated areas, developing the samples in their respective developer solvent causes the excess resin to dissolve. After the development step, only the wanted structures are left behind. Thus, by moving the voxel around the photoresist material, arbitrary 3D shapes can be obtained with submicron precision [37]. A schematic representation of the 2PP process is given in Figure 2.3. Around the voxel, the laser intensity passes the polymerization threshold and alters the material locally. Partly overlapping of multiple voxels allows the patterning of larger 3D structures. These structures are built by slicing (e.g., vertical distance) and hatching (e.g., horizontal distance) to individual voxel lines, which finally builds up to a larger structure after the exposure is completed.

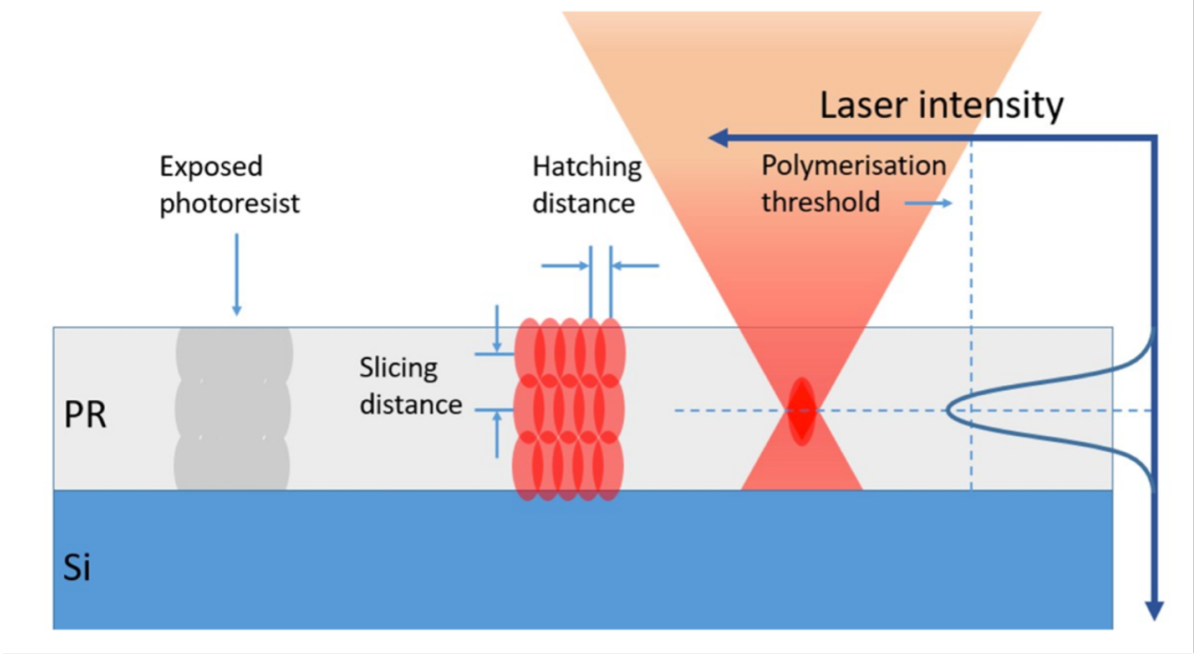

Figure 2.3: Schematic view of the 2PP process. The photoresist (PR) is polymerized at the focal point of the laser, also called the voxel. By moving this voxel around inside the material, arbitrary 3D shapes can be created. The distance between the voxel lines are expressed in hatching and slicing distance in horizontal and vertical direction, respectively. [15]

2.5. Applications

After successful fabrication of the photoresist-NDs composite and its patterning with 2PP, the technology may be used in a broad variety of applications. The 3D diamond loaded microstructures fabricated with the bottom-up approach can fulfill many roles, for example, as electrodes and structural material. The ease of fabrication allows the method to be used for rapid prototyping, as direct patterning offers a cost and time efficient alternative to the conventional top-down methods. Furthermore, elemental doping of the diamond with boron during the CVD process increases the electrical conductivity of the structures, making the properties of the boron-doped diamond (BDD) an exceptional choice as microelectrodes for electroanalysis and electrochemistry [38]. Examples of the possible future applications for these BDD electrodes are supercapacitors [39], micro-batteries in combination with carbon microelectromechanical systems (C-MEMS) [40] and biosensors [41]. The increased surface area provided with the proposed 3D diamond micro-patterning in combination with BDD can solve the largest bottleneck in the advance of BDD electrodes as an alternative to the porous electrodes currently prepared by methods that are difficult to reproduce [42]. Finally, the diamond loaded structures can be implemented as scaffold material in cell culturing experiments [43] or in microbiology [44].

3

Knowledge gap & research questions

The utilization of diamond films for the diverse range of future applications is partially limited due to the currently available diamond microfabrication methods. Both top-down and bottom-up diamond microfabrication methods are restricted to simple 2D and 2.5D structures. One of the limiting factors for the two manufacturing methods is defined by the seeding process, which is now highly dependent on relatively simple processes such as spin coating. In particular, the current seeding methods are not compatible with complex (3D) microstructures as the outer surface of the to-be-seeded microstructures is difficult to seed uniformly. Furthermore, seeding methods based on rotation of the samples or the immersion in liquids are likely to tear down the support structures that will hold the seeds. Therefore, the fabrication of arbitrary 2D and 3D diamond microstructures with the available seeding methods remains a challenge in the pursuit of the use of diamond structures in MEMS and other future applications.

In an attempt to solve this challenge, a method to fabricate 3D diamond coated structures using two-photon polymerized nanodiamond loaded photoresists is proposed. With this process, the possibility of single-step patterning of arbitrary complex 3D seeded microstructures is enabled. Adding a pyrolysis step after the 2PP process might improve the survival rate of the diamond loaded microstructures during the eventual diamond film growth by CVD. However, the combination of 2PP and pyrolysis with diamond NPs has yet to be explored.

Therefore, the aim of this study is to produce 3D microstructures composed of diamond NP loaded photoresist in order to form a base for future pyrolysis and CVD. Accordingly, the research question is "*What process is needed to manufacture diamond loaded photoresist microstructures using 2PP?*". To answer this question, the sub-questions "*what process is needed to suspend diamond NPs in the photoresist resin?*", "*what is the effect of the diamond NPs on the spin coating of the photoresist resin?*", "*what is the effect of diamond NPs on the 2PP of the photoresist resin?*", and "*what is the effect of diamond NPs on the mechanical properties of the photoresist resin?*" are addressed.

4

Project overview

This MSc thesis project, which encompasses the study of the formulation of NDs-loaded photoresist and the patterning of microstructures by 2PP, is part of a larger research project. The overarching project's goal is to develop a reproducible method for bottom-up microfabrication of arbitrary 3D core-shell glassy carbon and diamond micro-structures from nanodiamond loaded photoresist material using 2PP. This chapter starts with an overview of the overarching project plan and then zooms in on the objectives of the master thesis project, particularly the production of 3D microstructures composed of diamond NP loaded SU-8 photoresist. This production is highlighted by giving the various project steps and this chapter ends with a brief description of the systematic approach that is applied for the fabrication of the diamond-photoresist composite microstructures.

Project plan

The aim of the overall project is to obtain a reproducible method for bottom-up microfabrication of arbitrary 3D core-shell glassy carbon and diamond micro-structures from ND loaded photoresist material using 2PP. SU-8 is chosen as the photoresist material because of its widespread use and its compatibility with the fabrication of 3D microstructures through 2PP [45]. Furthermore, the pyrolysis of SU-8 structures leads to the formation of glassy carbon [45]. Moreover, glassy carbon is shown to be compatible with diamond growth on its surface through CVD [46]. Consequently, the compatibility of SU-8 with 2PP and pyrolysis makes it a suitable choice to use throughout the project.

A schematic view of the project is given in Figure 4.1, where three milestones are of importance. The first milestone is the successful formulation of the diamond NPs loaded resin. The second milestone is the successful patterning of the loaded resin with 2PP, and the third milestone is the successful production of core-shell microstructures after pyrolysis and CVD growth, respectively. The complete fabrication process thus comprises of multiple steps where different intermediates are created.

A six-step process is proposed to fabricate the glassy carbon and diamond core shell structures. First, a silicon substrate is pretreated with chemical cleaning (Figure 4.1, step 1). Afterwards, the diamond loaded resin is spin coated on the substrate (step 2). Then, the resin is patterned using a 2PP process with the *NanoScribe* (step 3). Hereafter, the substrate is developed to get rid of the excess resin (step 4), and pyrolyzed in an inert environment (e.g. Ar or N^2) to create the glassy carbon structures (step 5). This results in shrinkage of the written patterns and an increase in diamond NP concentration therein. In the final step, the glassy carbon structures are coated with a thin layer of polycrystalline diamond with the use of hot filament chemical vapor deposition (HFCVD) to create the core-shell architectures (step 6).

The scope of this master thesis is narrowed down to the creation of the diamond loaded resin and the 2PP of the microstructures (steps 1 to 4 in Figure 4.1, marked in red). During the extent of the project, the focus will be on the optimization of the loaded resin and the 2PP process by performing a systematic study of the effects of resin material and 2PP parameters on the as-produced microstructures. The different optimization parameters for the loaded resin and the 2PP process are shown in Figure 4.2. For the loaded resist, the diamond NP quantity (weight percentage, wt.%) and the viscosity of the resin are of importance. Adding different solvents and NDs drastically changes the properties of the resin. Therefore, a compromise must be sought where sufficient particles can be added to the resin without

decreasing the viscosity and 2PP printability. After the loaded resist is formulated, the laser power and scan speed of the 2PP process are optimized in order to successfully pattern microstructures with the loaded resin. To finally make the step towards the fabrication of 3D structures with multiple voxel lines, the slicing and hatching distances are optimized. After this information is obtained, the research questions can be answered.

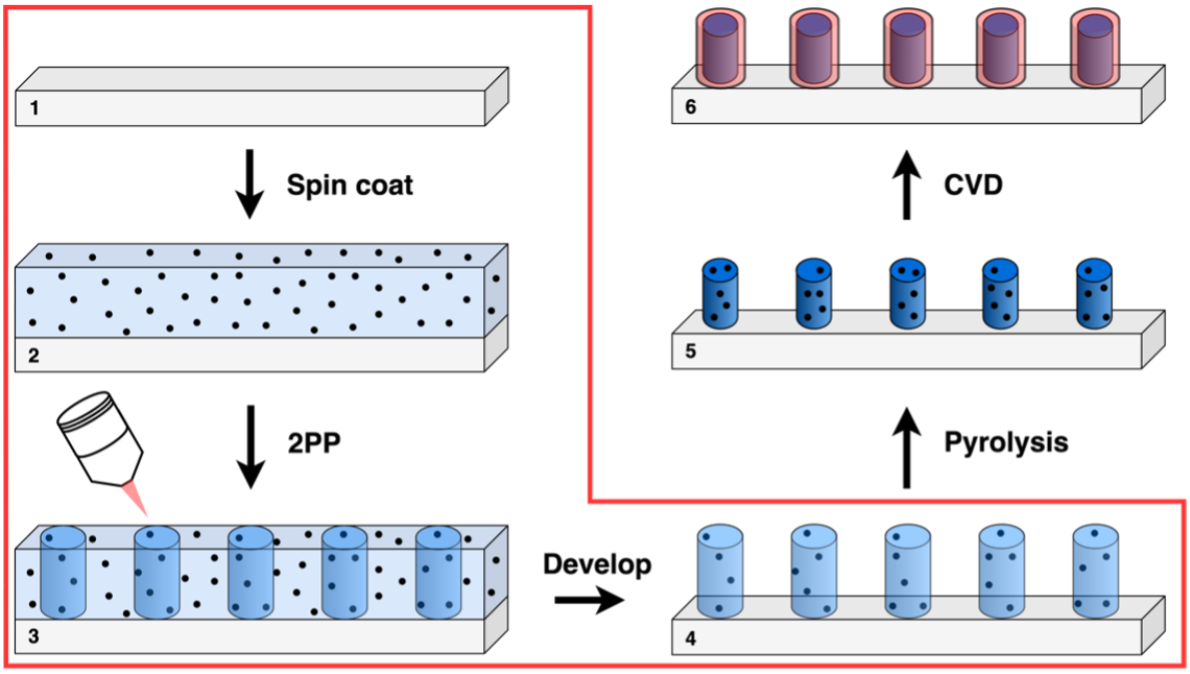

Figure 4.1: Schematic view of the fabrication method to obtain glassy carbon and diamond core-shell structures. A silicon wafer is cleaned (1) and coated with loaded resist (2). Then, structures are patterned with 2PP (3) and developed (4). Finally, the structures are pyrolyzed (5) and a surface layer of polycrystalline diamond is grown with CVD (6). The particular focus of this MSc project (i.e., steps 1 to 4) is marked in red.

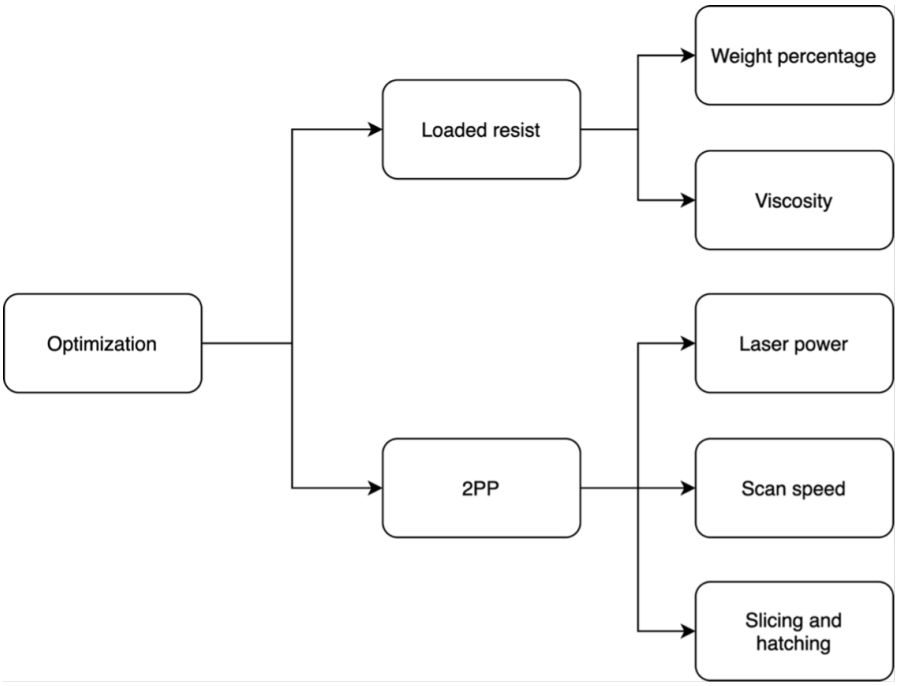

Figure 4.2: Schematic view of the optimization parameters for the formulation of loaded resist and 2PP process.

5

Materials and methods

To reach the goal of the production of nanodiamond loaded 3D microstructures using 2PP, a step-by-step procedure as depicted in Figure 4.1 was followed. The project was carried out in the Precision and Microsystems Engineering (PME) labs in the 3ME building of Delft University of Technology. This chapter gives detailed information about the different materials and methods used for the formulation of the loaded photoresist and the 2PP process. Finally, the characterization techniques used to quantify the loaded resin and microstructures produced by 2PP are described.

5.1. Materials

The base resin for the preparation of the diamond NP loaded photoresist was SU-8 (2000 series), which was purchased from *Kayaku Advanced Materials*. SU-8 is a negative tone epoxy-based photoresist resin. In particular, SU-8 is composed out of the Bisphenol A Novolac epoxy and Triarylsulfonium Hexafluoroantimonate salts photoacid generators (i.e., PAGs) in the solvent cyclopenthanone. The amount of solvent is defined by the type of SU-8, and is required to spin coat the SU-8 for 2PP. Depending on the amount of solvent, different thicknesses of SU-8 films could be obtained. SU-8 2007 and SU-8 2075 were used during the study. Uniform layers of 7 to 12.5 µm and 60 to 240 µm were be obtained with a single step spin coat process for SU-8 2007 and SU-8 2075, respectively.

Two formulations for the loaded resin were tried, first using dry diamond NPs in combination with SU-8 2007 and second using a nanofluid in combination with SU-8 2075. For the first part, the dry diamond powder uDiamond Molto, purchased from *Carbodeon (Finland)*, was used with SU-8 2007. These detonation originated unfunctionalized diamond NPs had a mean particle size of approximately 4.2 nm [47].

For the fabrication of the composite from SU-8 2075, a SU-8 compatible nanofluid was chosen. A solvent test was carried out in the available solvents (deionized) water, ethanol, isopropyl alcohol (i.e., IPA), acetone and 1-methoxy-2-propanol acetate (i.e., PGMEA). This solvent test showed that the developers acetone and PGMEA outperformed the other used solvents in dissolving SU-8 (see Appendix A). Due to this outperformance, the polymer compatible nanofluid RT-Ac-4 purchased from *Ray Techniques (Israel)* was used. This nanofluid was composed out of 4 wt.% highly dispersed diamond NPs in acetone. These NDs had sizes ranging from 3.5 to 6 nm [48]. The surface functionalization of the diamond NPs of the nanofluid (not specified by supplier but expected to be amine based) was designed to blend with High Impact Polystyrene, Acrylonitril-butadieen-styreen rubbers and other acetone soluble polymers. As anticipated from the solvent test, the carrier solvent acetone mixed well with SU-8. This coherence created by the solvent and the modified surface of the NDs made the nanofluid suitable to use in combination with SU-8.

5.2. Methods

The reader is referred to Figure 4.1 for a schematic overview of the various process steps for the production of the microstructures by 2PP. In the first two steps, a silicon wafer was cleaned and spin coated with loaded resist, respectively. After the spin coat process, the solvent was removed via a soft bake step. After soft baking, the resin solidified and became ready for 2PP. During the 2PP process, the PAGs reacted with the incoming laser light [49]. This reaction then electronically excited and de-

composed the PAGs locally. After 2PP, the sample was baked again to polymerize the material. When the temperature was elevated, the modified PAGs polymerized the epoxy resin by creating cross-links between the epoxy oligomers. This polymerization resulted in increased chemical resistance of the cross-linked areas to etching in PGMEA compared to the untreated areas. Accordingly, this difference in chemical resistance made it possible to remove the excess material and pattern the microstructures. Finally, after obtaining the microstructures, the loaded resin was compared to the base resin through morphological and mechanical characterization.

5.2.1. Preparation of the composite from dry powder

The loaded resin was first prepared using the dry powder, as this was initially thought to be the most suitable fabrication process. The process started by adding 1.7 grams of ND powder in 1.5 ml of SU-8 2007 in a centrifuge cap with 2 ml capacity. The closed cap containing the mixture was then sonicated by a *Fisher Scientific FB 15046* ultrasonic bath for 30 minutes. Hereafter, the suspension was centrifuged by an *Eppendorf 5415* centrifuge at 1000 rpm for 1 minute to remove the agglomerates.

5.2.2. Preparation of the composite from nanofluid

The preparation of the composite from the nanofluid was done by a five-step process as depicted in Figure 5.1. Step 1 entailed adding 5 ml of SU-8 2075 to a small glass vial with 10 ml capacity. Step 2 involved adding 2.5 ml of the nanofluid RT-Ac-4 to the closed vial and stirring on a *IKA RH basic* magnetic stirrer at 240 rpm for several hours. Step 3 included obtaining a homogenous mixture and opening the cap of the vial to evaporate the acetone inside the mixture for at least 48 hours. For this period, the suspension was still magnetically stirred. When roughly 90% of the acetone was evaporated, step 4 entailed stopping the magnetic stirring and heating the resin to 60 °C for one hour to remove the remaining acetone and regain its viscosity. Step 5 involved degassing the resin overnight in a low vacuum desiccator to remove the air bubbles trapped inside.

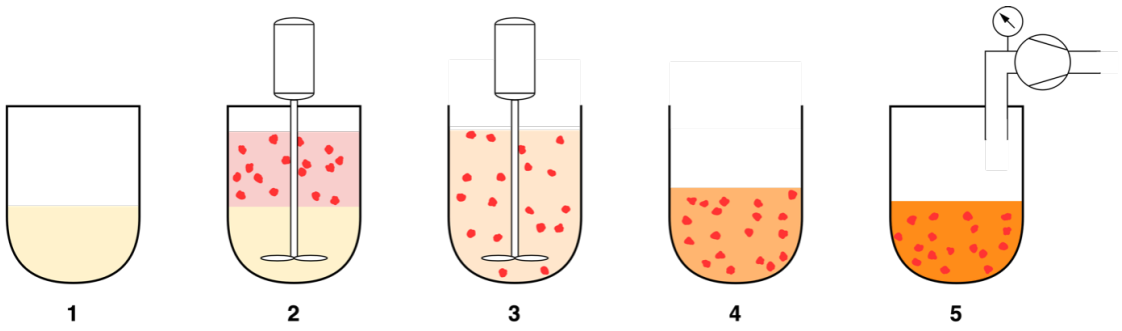

Figure 5.1: Schematic view of the process used to create the loaded resin. SU-8 2075 (yellow) was added to a closed glass vial together with the nanofluid (red) and stirred (steps 1 and 2). After a homogeneous mixture was reached (step 3), the cap of the vial was opened and the acetone was evaporated (step 4). Lastly, the mixture was degassed using a desiccator (step 5).

5.2.3. Preparation of the substrate

Before spin coating the loaded resin on the silicon substrates (2.5 x 2.5 cm^2), the substrate was pre-treated (Figure 4.1, step 1) to ensure adhesion between the resin layer and the substrate surface. First, the silicon substrate was chemically cleaned thoroughly by rubbing it with a soft cloth sprayed with acetone and then IPA. This rubbing was repeated for at least 5 times. Between each step, the substate was blow-dried using a nitrogen gun to evaporate the chemicals. After chemical cleaning, the substrate was treated with oxygen plasma in the *Diener Femto* plasma cleaner for 15 minutes at 80 W. The plasma cleaning process increased the hydrophilicity of the surface by terminating the surface with various oxygen-rich groups and dangling bonds. Lastly, the surface was silanized in a 3-(trimethoxysilyl) propyl methacrylate (i.e., MAPTMS) solution for at least 2 hours. Silanizing the substrates was done by submerging the substrates in a mixture of 150 µl MAPTMS and 30 ml ethanol inside a petri dish. The silanization process was added to promote the adhesion of the photoactive polymers to the silicon substrate by providing chemical bonds between the organic and inorganic interface, analogous to the effect between polydimethylsiloxane (i.e., PDMS) and glass [50].

5.2.4. Spin coat and soft bake

After the chemical treatment of the substrate, approximately 1 ml of loaded resist was poured on the substrate. Then, a three-step spin coat process (Figure 4.1, step 2) was used to obtain a homogeneous film of resin on the substrate using a *Laurell WS-400-6NPP-LITE* spin coater. The first step was to spin the substrate at 500 rpm for 10 seconds to spread the resin on the substrate. The second step was to ramp the rotation speed to the final spin value at maximum acceleration for 30 seconds to get a uniform film. This final spin value was dependent on the desired film thickness and lied between 1000 and 4000 rpm. Finally, the edge bead at the corners of the substrate was gently removed by a soft cloth sprayed with acetone. Removal of the edge bead was essential to prevent the backflow of resin towards the center of the substrate and keep a uniform layer at the printing area.

After the spin coating process, the solvent was evaporated from the spin coated layer by soft baking the substrate on a level hot plate. For this purpose, the available *Polos 150S* hot plate was used. To reduce the stress accumulation inside the film, a two-step heating process was used. The temperature was first gradually raised from room temperature to 65 °C, with a temperature gradient of 1 °C/min. With increasing temperature, the viscosity of the film slowly decreased, allowing the remaining air bubbles that were trapped inside resin to escape. The substrate was then held at 65 °C for 15 minutes. Hereafter, the temperature was again ramped with the same gradient to 95 °C and left for at least 30 minutes to ensure a smooth film. Lastly, the substrate was cooled back to room temperature on a cooling block to finalize the process. After holding the substrate for at least 15 minutes at room temperature, the substrate was considered ready for the 2PP process.

5.2.5. Two-photon polymerization

The microstructures were printed using a *Nanoscribe (Photonic Professional GT, Germany)* system in oil-Dill mode as shown in Figure 5.2. For the 2PP process (Figure 4.1, step 3), the spin coated resin layer was covered with a few droplets of *Zeiss Immersol 518F* oil. The objective lens *(Plan-Aprochromat 63x, Zeiss)* was immersed in the oil to provide a liquid interface to the incoming laser with a similar refractive index as compared to the resin, which was 1.518 and 1.58, respectively. This oil interface reduced the undesired effects of air-resin interfaces. Also, this configuration protected the objective from damage that may have occurred from contact with the objective on the hard resin surface. Furthermore, the silicon substrate was not transparent to the 780 nm laser of the *NanoScribe*. Therefore, the interface between the silicon and loaded resin was easily found.

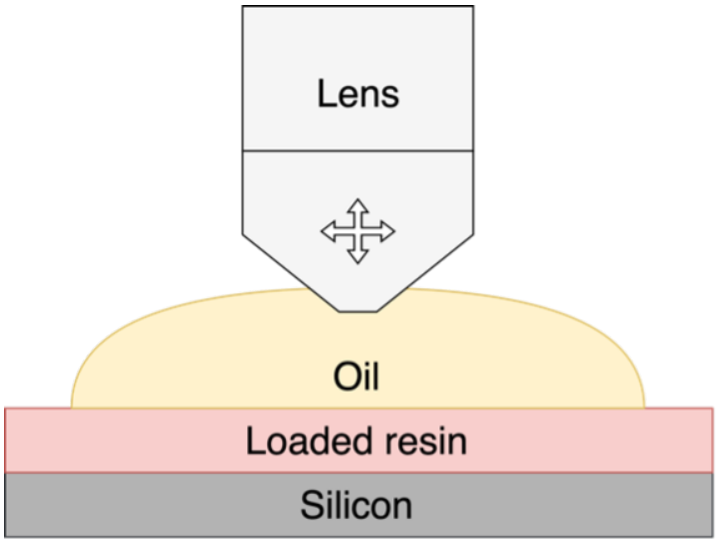

Figure 5.2: Schematic view of the conventional configuration method used to pattern the microstructures. The objective lens was submerged in oil that covered the loaded resin on the silicon substrate.

5.2.6. Post-exposure bakes and developing

After the 2PP process, the PAGs were activated by elevating the temperature (Figure 4.1, step 4). Therefore, the substrate was gradually heated to 65 °C with a temperature gradient of 1 °C/min. The substrate was left at 65 °C for 15 minutes. Then, the temperature was gradually heated with 1 °C/min to 95 °C and left for 15 minutes. This was followed by cooling the substrate for 15 minutes on a cooling block to finalize the cross-linking process. Hereafter, the substrate was developed by submerging in PGMEA for several minutes. This duration was dependent on the spin coat thickness and took 10 minutes. After the development step, the PGMEA was washed off in an IPA bath for 2 minutes and subsequently blow dried with an air gun on low pressure. The PGMEA dissolved the excess SU-8 resin and left the cross-linked patterns untouched, finally resulting in the patterned diamond loaded microstructures.

5.2.7. Characterization of results

To evaluate the production of nanodiamond loaded 3D microstructures, the loaded resist and the obtained microstructures (both loaded and unloaded) were analyzed by a series of measurements. For the loaded resist, the dispersion characteristics of the NPs were analyzed through dynamic light scattering (DLS) using a system available at the faculty of applied sciences (TNW). Details about this setup can be found in the previous study by Wang and colleagues [51]. The geometric characteristics of the fabricated microstructures were analyzed with a *Jeol JSM-6010LA* scanning electron microscope, a *Bruker Contour GT-K 3D* white light interferometer and a *Keyence VHX-6000* optical microscope. Fluorescence microscopic imaging of the microstructures was performed on a *Zeiss Axio Observer* fluorescence microscope. Finally, the mechanical properties were determined using the *Femtotools FT-NMT03* mechanical testing setup.

6

Results

This chapter provides an overview of the important findings on the formulation of the loaded resin and its microfabrication. First, the preparation of the loaded resin and its characterization through DLS and fluorescence microscopy is elaborated. Then, the 2PP process is presented by discussing the optimization of low aspect ratio pillars, and the build-up towards the optimization of pillars with higher aspect ratios. The 2PP process is followed by the morphological and mechanical characterization of the obtained microstructures.

6.1. Preparation of the loaded resin

The preparation of the loaded resin was formulated first by using the dry powder approach. However, the presence of many large agglomerates limited the reproducibility and performance of the resin as illustrated in Appendix B. The necessity of the centrifuge step to separate the larger agglomerates restricted the batch size to small 2 ml centrifuge caps. This small batch size combined with the difference in sedimented diamond NPs after centrifuging gave uncertainties in terms of diamond concentrations and their dispersion for every print. Possible reasons for the agglomeration of the NDs in the prepared composite were the presence of larger clusters of NPs in the detonation originated dry powder source [35]. Furthermore, the low power output of the sonication bath may have been insufficient to fully disperse the NDs added inside the resin. Hence, a different approach using a nanofluid was selected at the initial phases of the project to prepare the loaded resin. For this reason, the upcoming paragraphs will only treat the characterization of the loaded resin fabricated from the nanofluid.

The formulation of the loaded resin from the diamond nanofluid was based on a tradeoff between the ND concentration and the viscosity. Adding more nanofluid resulted in higher concentrations of NDs, at the expense of an overall decrease in dynamic viscosity and an increase in liquid density. A similar effect was seen by Loos and colleagues [52] where an addition of 10 wt.% of acetone decreased their epoxy resins viscosity by almost 50%. Consequently, obtainable spin coat thicknesses decreased gradually for the added nanofluid, thereby reducing the printing window drastically. Furthermore, the increased liquid density resulted in intensified bubble formation during the pre-bake process. These bubbles, which were caused by the evaporation of the solvents, created voids inside the layer and resulted in an inhomogeneous surface. Moreover, remaining acetone altered the cross-linking process of the resin negatively, possibly resulting in poorer properties as compared to the base resin [50].

The negative consequences of remaining solvents inside the resin was prevented by evaporating the acetone out of the loaded resin before the spin coat and pre-bake processes. The acetone was evaporated slowly at room temperature to prevent the possible agglomeration of the NPs due to the sudden evaporation of the carrier solvent. The evaporation was carried out while magnetically stirring the loaded resin to ensure homogeneity, and prevent the resin from drying out locally. The evaporation of the acetone was successfully performed in to a volume fraction of 33% acetone nanofluid in SU-8 2075, where 2.5 ml of nanofluid was added to 5 ml of SU-8. The further addition of the nanofluid required evaporation times exceeding 48 hours. During these 48 hours, skins of dried out resin were formed on the resin surface. Therefore, the maximum achievable weight percentage with the used single-step evaporation process was approximately 1 wt.% of NDs on dry SU-8 epoxy after the pre-bake step.

The evaporation step with magnetic stirring the loaded resin introduced micrometer sized air bubbles that manifested inside the resin. These bubbles taunted the manufacturability and reproducibility of the microstructures later during the 2PP process by introducing surface irregularities and pores. This taunting destroyed the microfabricated pillars as shown in Appendix C. Although not fully removed, the encapsulated air bubbles were reduced by heating the resin up to 60 degrees C for one hour and degassing in a low-vacuum desiccator overnight. Followed by obtaining an almost acetone free ND containing loaded resin.

6.1.1. Characterization of loaded resin – Dynamic light scattering

After obtaining the resin, the average size and dispersion characteristics of the NPs were analyzed by DLS. For DLS analysis, two different loaded resins of 0.5 and 1 wt.% were prepared to look for possible differences in dispersion characteristics for increased ND percentage. The working principle of DLS is based on particles undergoing Brownian Motion inside a quiescent fluid [53]. During the DLS measurement, a laser light is shined on the target and gets scattered by the floating particles. This scattered laser light is then collected at a 90-degree angle, where the intensity of the collected laser light gives information about the average hydrodynamic size and dispersion characteristics of the particles inside the resin. This information is derived from the Stokes-Einstein equation and is dependent on the solvent's refraction coefficient and viscosity values.

DLS measurements were performed on both loaded resins (0.5 & 1 wt.%), SU-8 2075 and the nanofluid (see Appendix D). Figure 6.1 gives an overview of the results obtained by the DLS measurements. The intensity data is normalized for all the plots, thereby only giving information about the most dominant peaks. The acetone nanofluid showed a narrow-size distribution around 70 nm. The same behavior was found regarding the two loaded resins, where narrow peaks are located around 20 nm. Therefore, this preliminary DLS data hint towards a monodispersed ND loaded resin without the presence of large agglomerates. However, the measured particle sizes deviate from the expected values of around 4 nm as provided by the supplier. Possible causes for this dissimilarity were the differences in the medium parameters, such as its refractive index and viscosity. Moreover, the measured hydrodynamic size included the influence of the surfactant shell formed around the NPs [54]. As the surface of the NDs were functionalized, the surfactant shell moves along with the NPs and shifts the values for the measured hydrodynamic size as compared to the actual size. When examining the SU-8 (black) graph, two wide peaks can be seen around 60 and 1000 nm. No response was expected considering that no particles were present inside the base resin. Therefore, the origin of these wide peaks is unknown and was likely caused by poor calibration of the DLS system for this resin. A negative bias might be formed towards the disappearance of the influence of the SU-8 (black) peaks at the loaded resins. However, this contribution of the black graph may be hidden behind the more dominant peaks due to the normalization of the data.

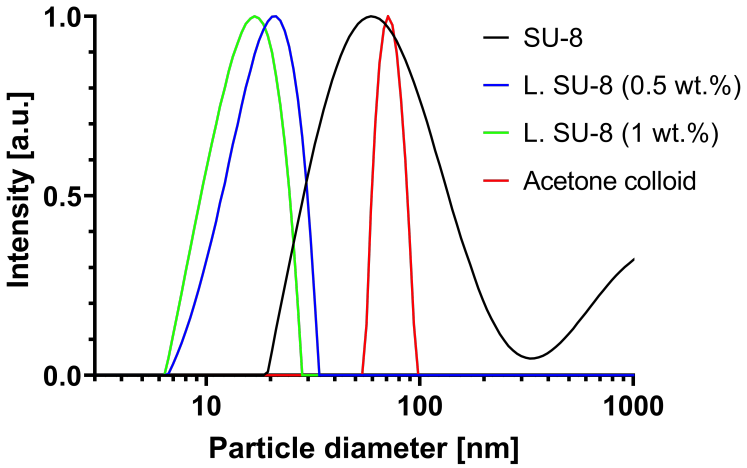

Figure 6.1: Particle size distribution plots of SU-8 (black), loaded SU-8 with 0.5 wt.% ND (blue), loaded SU-8 with 1 wt.% ND (green) and the acetone nanofluid (red), as obtained by DLS measurements.

Measuring colloids through DLS proved to give difficulties regarding reproducibility and reliability. Following the remarks described by Osawa [55], the DLS system should be calibrated before each measurement for changing medium and measured multiple times in order to obtain a more accurate representation of the real sizes and distribution of the NPs. Additionally, the reliability can be further improved by measuring and including the viscosity and refractive index of the fluids in the calculations. However, due to the limited accessibility of the DLS setup at another faculty, the measurements could not be redone in the available timeframe.

6.1.2. Characterization of loaded resin – Fluorescence microscopy

Further analysis on the loaded diamond films was examined by a fluorescence microscopy. During fluorescence microscopy, the sample was excited by a light source with a selected wavelengths of 385 (UV), 475 (blue), 555 (green) and 630 nm (red). After excitation, the sample emits an fluorescence signal typically at a shorter wavelength as compared to the excited signal (i.e., Stokes shift) [56]. The intensity of the fluorescence signal was collected through four passbands, this being blue (425 ± 30 nm), green (514 ± 30 nm), yellow (592 ± 25 nm) and red (709 ± 100 nm). The collected signals were measured separately and combined afterwards, thereby giving a visual representation of the emitted signal.

Samples of loaded and unloaded resin were spin coated on a silicon substrate and baked to get insight on the behavior of the NDs after the spin coat and soft bake processes. To provide a background for the measurements, a few droplets of the acetone nanofluid was dispensed on a glass microscope slide and dried to evaporate the solvents. Hereafter, the samples were analyzed by fluorescence microscopy. Unloaded SU-8 gave a strong mixed fluorescence response for UV excitation, making it difficult to differentiate between the fluorescence contribution of the SU-8 and the NDs. Therefore, the blue light was used to analyse the effect of the NDs on the fluorescence emittance. The measurements gave visible differences of emitted fluorescence signals for blue excitation light as depicted by Figure 6.2. The first column of images shows the emitted response of the loaded resin (a), the unloaded resin (c) and the NDs (e). The second column shows the corresponding intensity plots of the emitted responses for the loaded resin (b), the unloaded resin (d) and the NDs (f). The loaded resin emitted a homogenous green fluorescence color, whereas the base resin had no fluorescence signal besides noise. The NDs emit a mixture of red, green, and yellow light, translated to a bright yellowish color. Due to the droplet formation of the nanofluid prior to evaporation, the fluorescence response of the NDs is inhomogeneous.

The fluorescence of NDs are related to the existence of N3, H3 and NV^- centers, responsible for the emittance of blue, green, and red fluorescent light, respectively [57, 58, 59, 60]. The effect of the N3 centers was not visible in any of the measurements including the lower wavelengths. For the measurements of the loaded resin, the green fluorescence caused by the H3 centers is predominant. It can also be seen that the color is homogenous, thus hinting towards an uniform dispersion of the NDs throughout the spin coated resin. The yellowish color emitted from the NDs are likely caused by the coexistence of NV^- and H3 centers. The difference between the loaded resin and NDs might be a result from the lower concentration of NDs inside the resin. Furthermore, remaining solvent and/ or the epoxy groups may have played a role in suppressing the NV^- vacancy, and therefore only showing the green color. However, the exact reason for the disappearance of the red emittance signal was not discovered and more research needs to be conducted to track down the origin of this difference in color response.

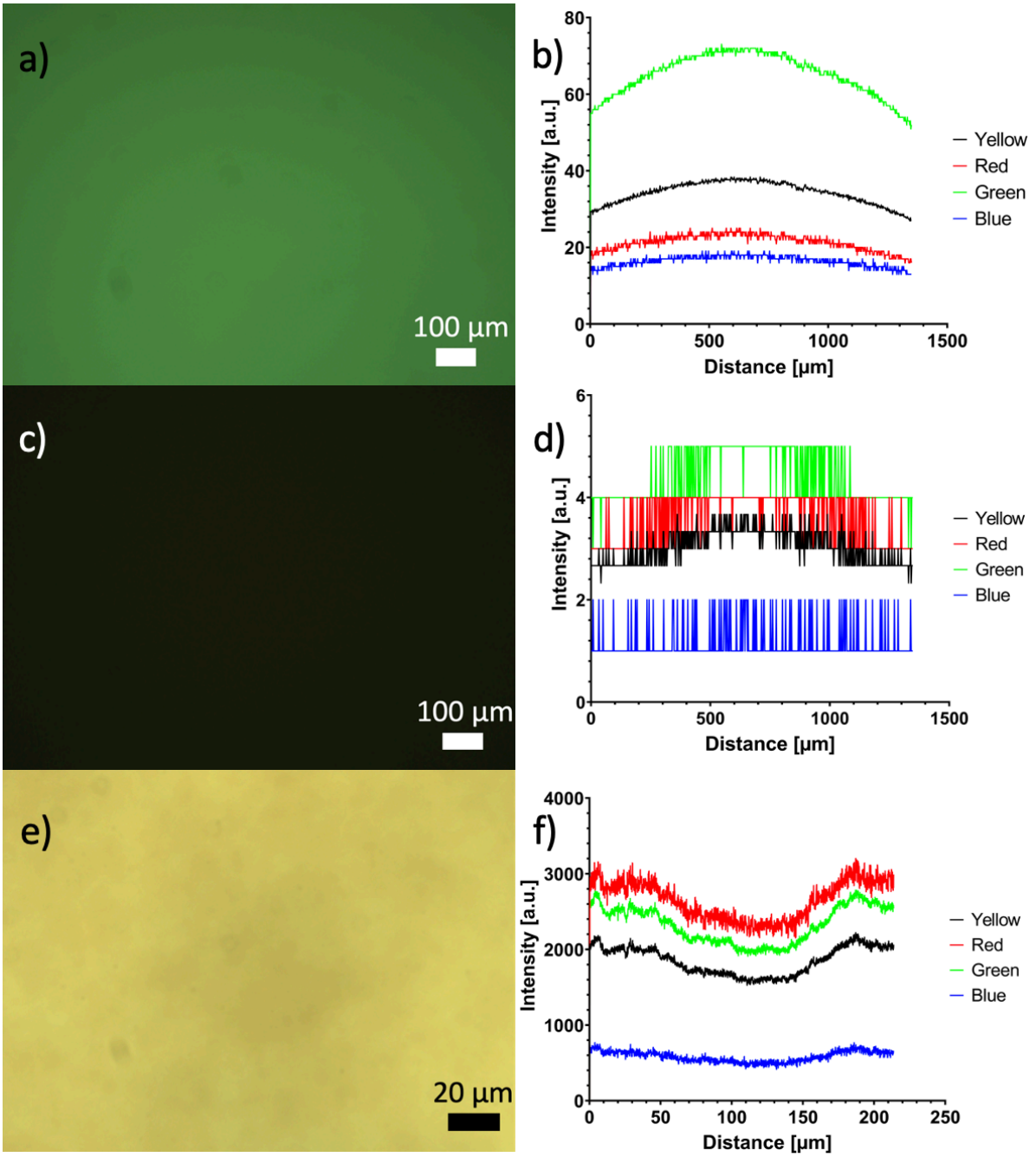

Figure 6.2: Fluorescence responses of spin coated and hard baked ND loaded SU-8 (a), unloaded SU-8 (c) and NDs (e), together with their corresponding intensity plots for loaded resin (b), unloaded resin (d) and NDs (f).

6.2. Optimization of two-photon polymerization

After obtaining the loaded resin and confirming the dispersion characteristics, the step towards the fabrication of microstructures using 2PP was made. At first, low aspect ratio pillars were optimized using the loaded resin obtained by the dry powder method (0.9 wt.% or 0.3 volume% ND). Hereafter, the fabrication of pillar arrays with higher aspect ratio was optimized using the loaded resin originated from the nanofluid method (1 wt.% or 0.4 volume% ND).

6.2.1. Low aspect ratio pillars

The optimization process for the low aspect ratio micropillars was based on the laser power, scan speed and sizes of the pillars. The hatching and slicing distances were kept constant at an in-house standard value of 0.3 μm for SU-8 2007. Due to the viscosity of the SU-8 2007, the maximum obtainable layer thickness was 12.5 μm with a single step spin coat process. The surface of the spin coated layer from the loaded resin was not completely uniform because of remaining impurities in the resin, causing a wavy pattern. Therefore, to decrease the effects of this imperfect surface, a maximum height of 8 μm was kept for the pillars.

Pillars with diameters of 5, 10, 25 and 50 μm were printed using the *NanoScribe*. A dose test was performed with pillars in arrays with increasing laser power (vertically) and scan speed (horizontally), as shown in Figure 6.3. The laser power was varied from 20 to 45% (of 50 mW) with increments of 5%, and the scan speed from 2 to 8 mm/s with increments of 1 mm/s. Zooming in to the area of the 25-micron pillars as shown in Figure 6.4, four zones can be distinguished. In the red areas, the pillars are burned entirely as seen from the black color. At the yellow regions, the structures are partly burned and troubled by bubble formation. The pillars in the green region are optimal in terms of bubbles formation. Furthermore, it can be noted that on average the size of the bubbles grows with increasing laser power, and the number of bubbles increases with decreasing scan speed. Moreover, larger pillars tend to burn with lower doses as compared to smaller pillars. Therefore, one extra column was added for the 50-micron pillar array.

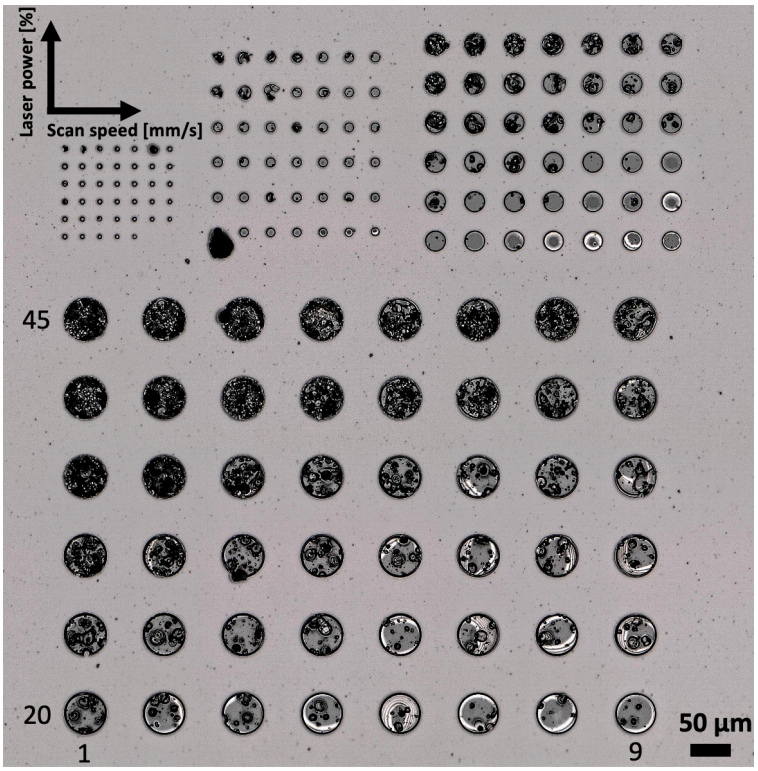

Figure 6.3: Optical image of the printed micropillar arrays of 5, 10, 25 (from left to right, respectively) and 50 μm (below). The laser power and the scan speed was increased on the vertical and horizontal axis, respectively.

The bubble formation is likely caused by the difference in refractive index and reflectivity of the NDs and resin. Diamond has a higher refractive index (2.41) compared to the used resin (1.58 for SU-8). For this reason, the NDs react different to the incoming laser light. The resin, as prepared by the dry powder method, contained a large number of agglomerates, which blocked and absorbed incoming laser light partially. This effect created local hot spots and in turn partially decomposed or burned the resin locally, creating bubbles in the process. This effect was increased for larger structures as heat accumulation played a dominant role for longer print times.

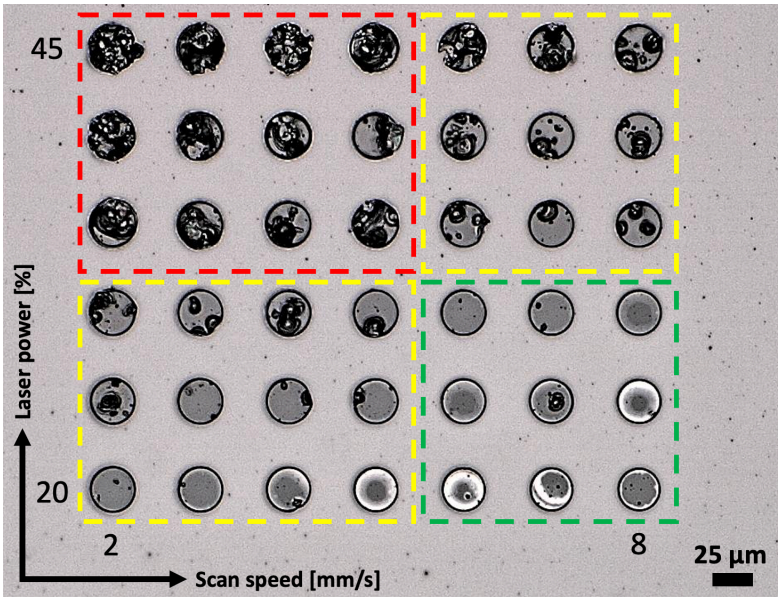

Figure 6.4: Zoomed in optical image of the 25 μm pillar array from Figure 6.3. The image distinguishes four zones. The laser power and the scan speed was increased on the vertical and horizontal axis, respectively.

Concluding from Figures 6.3 and 6.4, reduced bubble formation was seen for low laser power (<20%). To provide enough energy to polymerize the resin, this low laser power should be coupled with low scan speed (<2 mm/s), which increases the print time drastically. Because of the increased print time and heat accumulation for large pillars (50 μm), smaller pillars of 20 microns were used for the next part of optimization of pillars with larger aspect ratios.

6.2.2. Higher aspect ratio pillars

The optimization for higher aspect ratio micropillars was performed on micropillars of 20 microns in diameter and height. This height was selected in order to decrease the printing time, and still keeping an aspect ratio of 1. Because of the implications related to the agglomeration formation, the loaded resin created by the nanofluid method was used for this part of the optimization. Analogues to the low aspect ratio method, the laser power and scan speed were optimized first with a slicing and hatching distance of 0.3 μm. After finding an optimal range of values for the laser power and scan speed, the slicing and hatching distances were varied. As relatively low doses were used to print the microstructures, a MAPTMS substrate surface treatment was used to improve the adhesion of the patterns to the substrate. Hereafter, the loaded resin was spin coated first at 500 rpm for 10 seconds and then at 2000 rpm for 30 seconds. WLI analysis showed that a layer of about 75 microns was obtained.

To optimize the pillars with a diameter and height of 20 microns, a micropillar array as shown by the SEM image in Figure 6.5 was fabricated. On the vertical axis, the laser power was varied from 11 to 17% with increments of 1%. The scan speed was varied on the horizontal axis from 0.2 to 12 mm/s with increments of 0.05 mm/s. The optimal pillars were found in the area marked by the ellipse. The area on the left side of the ellipse was covered mainly with burned pillars, whereas the area on the right side was dominated by underexposed and delaminated pillars.

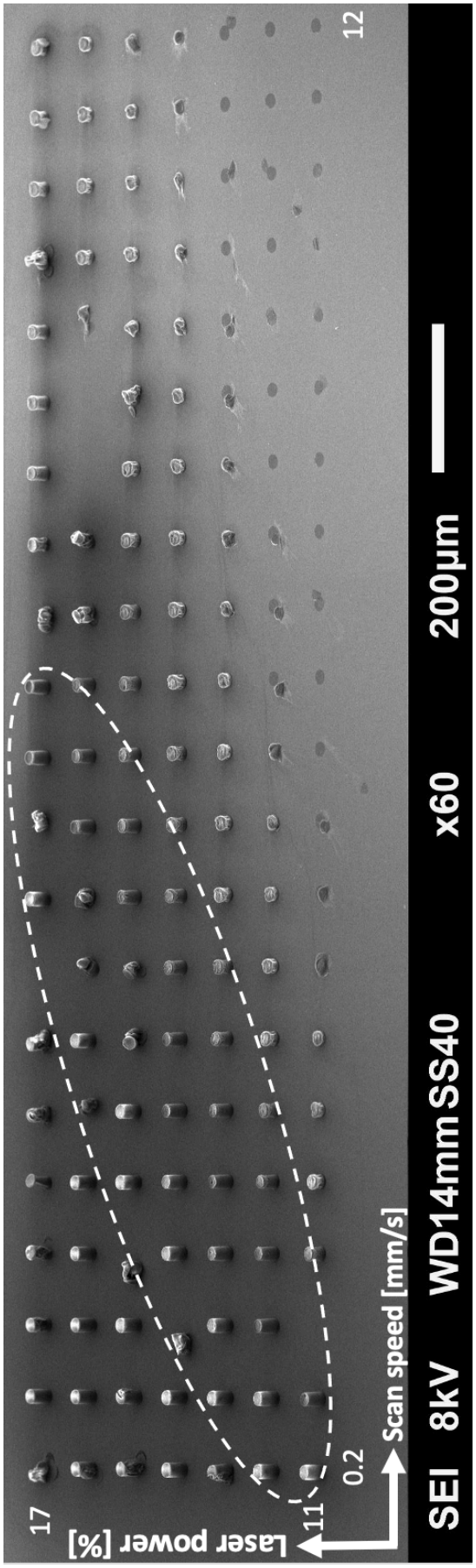

Figure 6.5: SEM image of the micropillar array used to optimize the laser power and scan speed of pillars with a diameter and height of 20 microns. A constant slicing and hatching distance of 0.3 microns was used.

Close-ups of the area around the ellipse are shown in Figure 6.6. Partially burned pillars were seen at the left side outside the ellipse (a) and underexposed pillars at the right side (b). In the middle of the ellipse (c), the pillars were based at the middle of the two extremes, displaying both burned and underdeveloped characteristics. The optimal pillars in terms of appearance were found for the lowest laser power and lowest scan speed at the bottom left side (d), corresponding to a laser power of 12 to 14% and a scan speed of 0.2 to 0.3 mm/s. The shifts in color and dimensions occurring at the surface of the pillars were caused by charge accumulation from the SEM and not by defects.

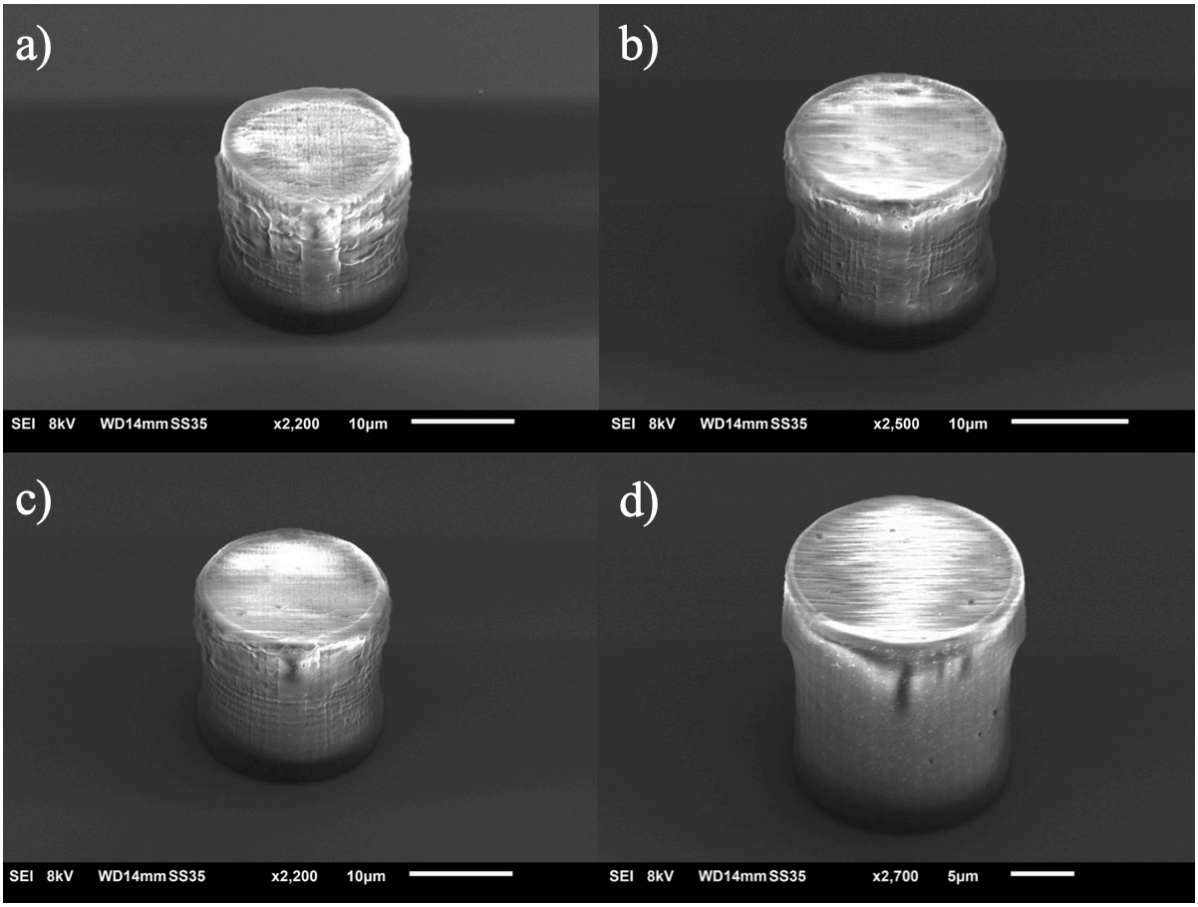

Figure 6.6: Zoomed in SEM images of pillars around the ellipse from Figure 6.5. The image shows partially burned (a) and underexposed (b) pillars from the outside regions of the ellipse, and pillars located in the middle (c) and bottom left side (d) inside the ellipse.

After obtaining the optimal laser power and scan speed range, iterations have been done for the slicing and hatching distances. It was noted that the variation of slicing distance gave no significant change for the outer surface. In contrast to the slicing distance, the difference for the hatching distance was visible from the top as depicted by Figure 6.7. This figure shows the pillars with a slicing and hatching distance of 0.2 micron (a) and 0.3 micron (b). The pores were caused by air bubbles which remained inside the resin after the baking processes.

Smaller hatching distances resulted in pillars with decreased roughness as the distance between the voxel lines became smaller. By this decrease in roughness smoother pillars with increased structural integrity were formed. However, this change in writing parameters extended the print time by 1.5 times each for slicing and hatching. Then, a tradeoff was made by choosing the slicing distance of 0.3 micron and hatching distance of 0.2 microns so that the writing time would not increase more than necessary. This tradeoff was combined with a laser power of 14% and a scan speed of 0.2 mm/s. The followed try-outs with the optimized parameters led to 3D microstructures with features sizes of 2 microns and aspect ratios of 1:5. SEM images of these 3D microstructures can be found in Appendix E.

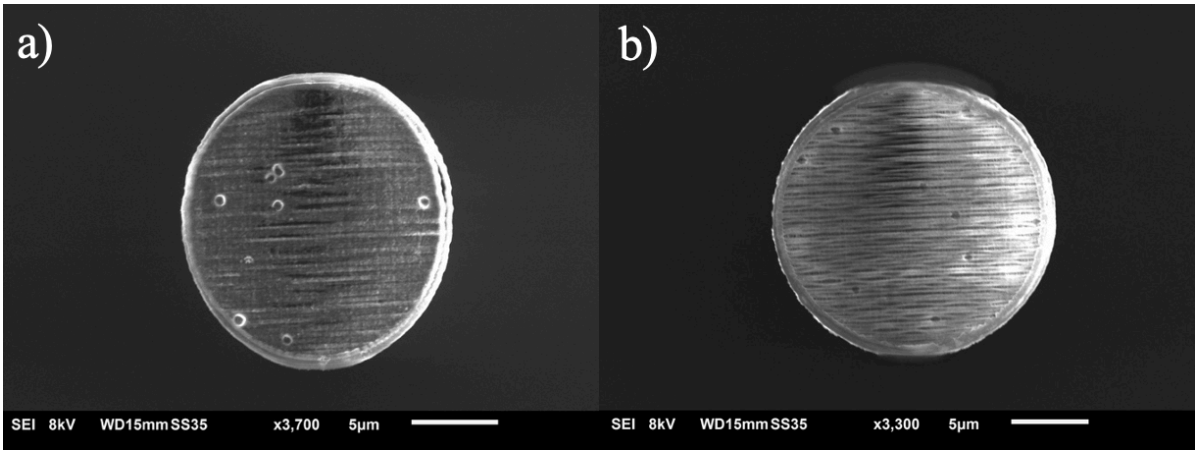

Figure 6.7: SEM images from the top surface of pillars with a slicing and hatching distance of 0.2 micron (a) and 0.3 micron (b).

6.3. Characterization of pillars

To get insight on the properties of the optimized pillars, characterizations were done on pillar arrays with diameters and heights of 20 microns. The difference between pillars fabricated from loaded resin and unloaded SU-8 2075 resin were analyzed by creating samples of both resins with the same process parameters. To match the layer thickness of the loaded resin, SU-8 2075 was spin coated first at 500 rpm for 10 seconds and then at 3000 rpm for 30 seconds. This resulted in a thin layer of unloaded resin of around 75 microns.

After the fabrication of the pillar arrays with both resins through 2PP, morphological characterization was conducted through SEM and WLI analysis. Then, the dispersion of the NDs within the microstructures after 2PP was evaluated by fluorescence microscopy. Lastly, the mechanical properties of the pillar arrays were measured by compression test with the Femtotools by using the 50x50 μm^2 silicon tip.

6.3.1. SEM and WLI

Figure 6.8 displays the characterization of the loaded (a) and unloaded (b) pillars through SEM analysis. No large dissimilarities were visible from the images. However, the pores caused by the air bubbles remained present in the loaded pillars. Again, it should be noted that the changes in color in the images were caused by charge accumulation during SEM imaging.

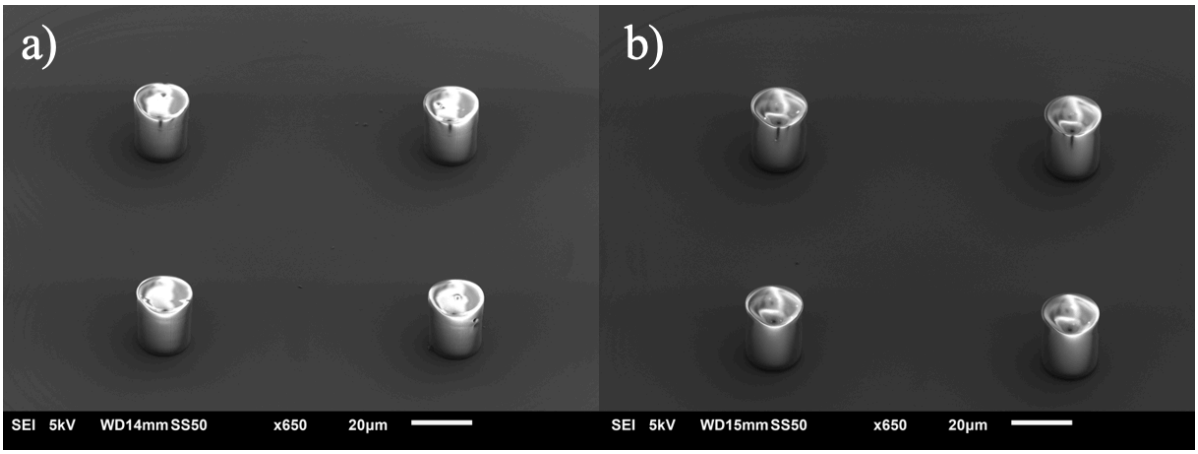

Figure 6.8: SEM images of loaded (a) and unloaded (b) pillar arrays, fabricated with the same process parameters.

After SEM analysis, the topological properties of the pillars were measured using WLI. Figure 6.9 gives an overview of the WLI results for one unloaded pillar. The 3D representation (a) of the pillar shows a gradient along the height of the pillar, where the diameter of the pillar becomes smaller for increasing length. This gradient effect on the diameter is also visible from the top view (b). Height profiles (c) along line 1 and 2 as illustrated on the top view indicate that the pillar is approximately 21 microns at the base and around 18 microns at the top. The total height of the pillar was around 23.2 microns. Furthermore, zooming in to the surface of the top side (d) display a maximum peak-to-valley roughness of around 700 nm.

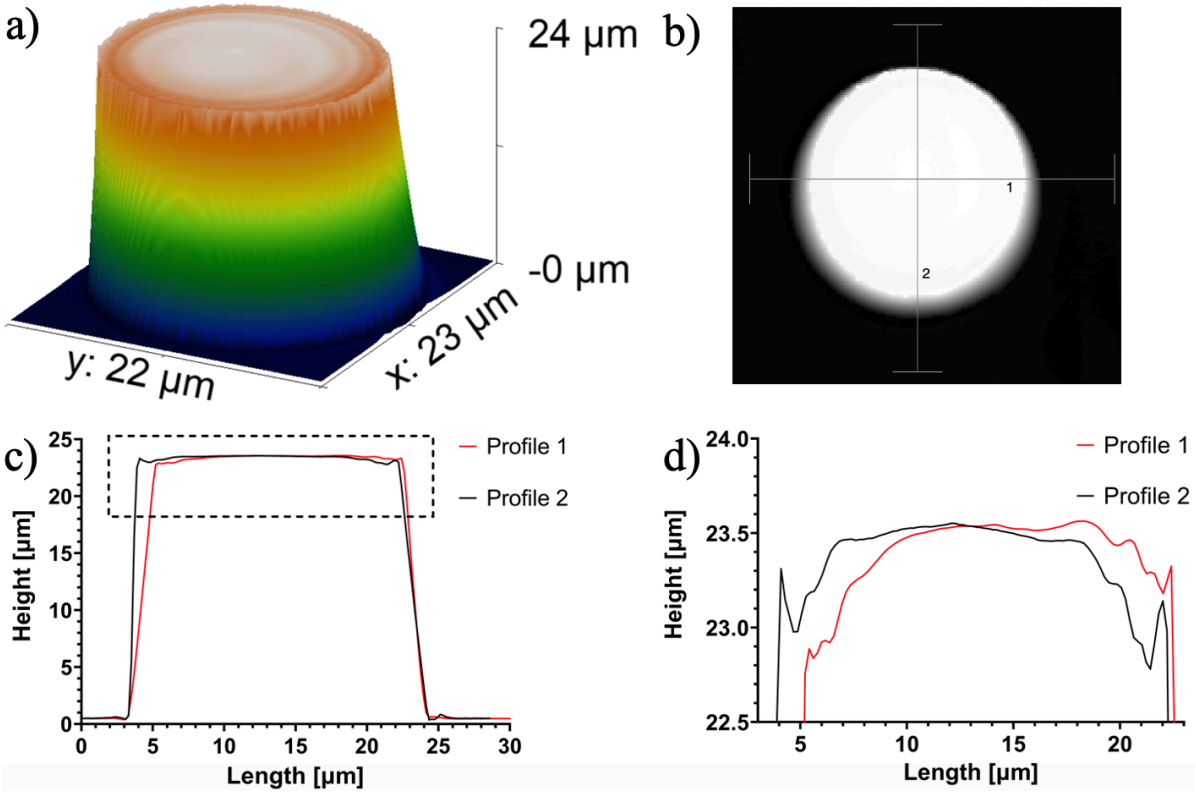

Figure 6.9: Topography information of a unloaded pillar obtained by WLI, showing its 3D representation (a) and top view (b). Furthermore, graphs of the height profiles (c and d) along the lines shown in the top view are displayed.

The same topological analysis was done on loaded pillars as shown in Figure 6.10. The 3D representation (a) shows a straighter gradient compared to the unloaded pillar. This absence of gradient is also visible from the top view (b). The height profile (c) indicated a shorter height of around 21.6 microns, with a diameter of around 20 microns along the length of the pillar. The close-up (d) displayed a maximum peak-to-valley roughness of around 300 nm, which is significantly smoother as compared to the unloaded pillar. It should be noted that the transparency of the surfaces for loaded pillars was lower, thereby giving a more accurate representation for the loaded pillars as compared to the unloaded pillars.

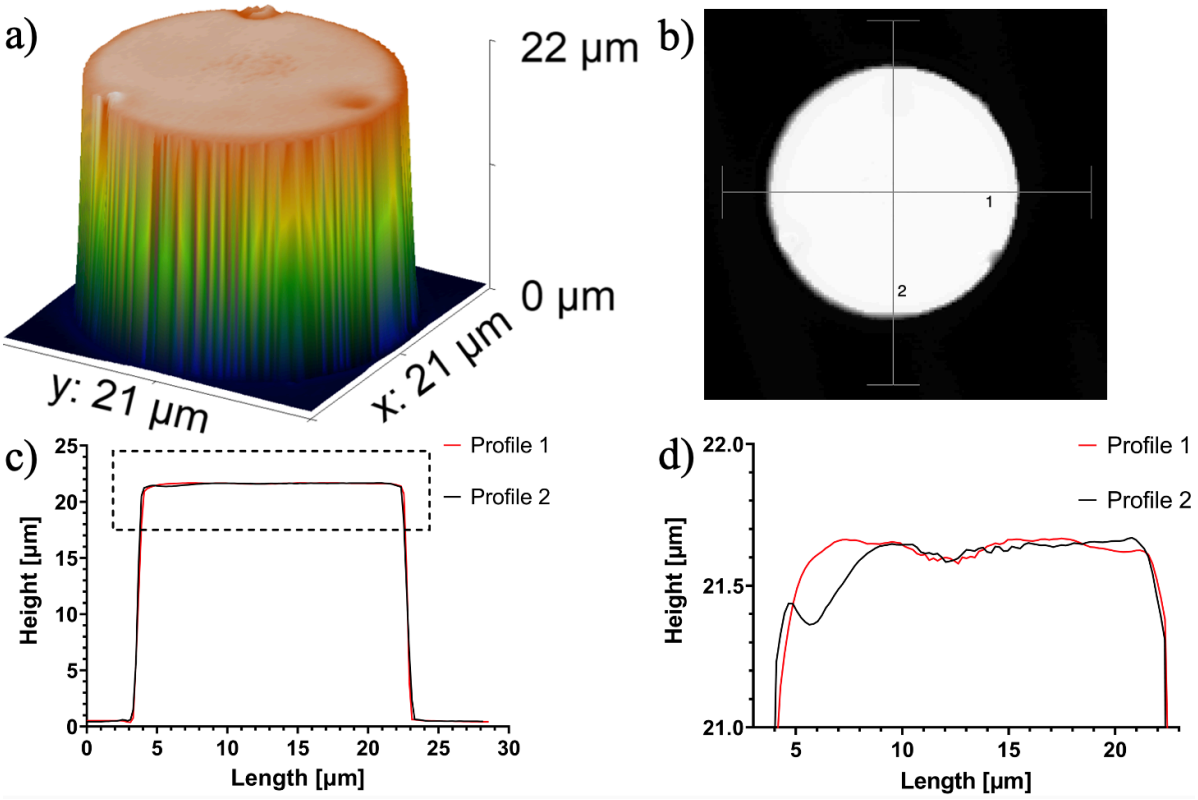

Figure 6.10: Topography information of a loaded pillar obtained by WLI, showing its 3D representation (a) and top view (b). Furthermore, graphs of the height profiles (c and d) along the lines shown in the top view are displayed.

6.3.2. Fluorescence microscopy

The difference in transparency during the WLI measurements was likely caused by the presence of NDs inside the pillars. To get a better view on the presence and dispersion of these NDs, both loaded and unloaded pillars were analyzed through fluorescence microscopy. The samples were excited with all of the available wavelengths (UV, blue, green and red) and their fluorescence signal was measured. Again, the blue laser was used analyse the effect of the NDs on the fluorescence response because of the lower emittance contribution of SU-8. Figure 6.11 shows the fluorescence responses of the loaded (a) and unloaded (b) pillars after excitation with the blue laser. A vague fluorescence signal was collected for the unloaded pillar, whereas the loaded pillar emitted a homogeneous yellow light in contrast to its black background. The intensity plots as taken on the dashed lines (in a and b), indicate a mixed response of all colors for both the loaded (c) and unloaded pillars (d).

Cross-linked SU-8 is known to have a fluorescence response [61], causing the low emittance signal as shown in Figure 6.11b. Thus, the fluorescence response of the loaded pillar is a combination of the contribution of the SU-8 and the NDs. The similarities in fluorescence response of the loaded pillars with respect to the NDs from Figure 6.2 (c & f) hint towards the successful incorporation of the NDs inside the pillars. The homogenous color indicated an even distribution of the NPs throughout the pillar.

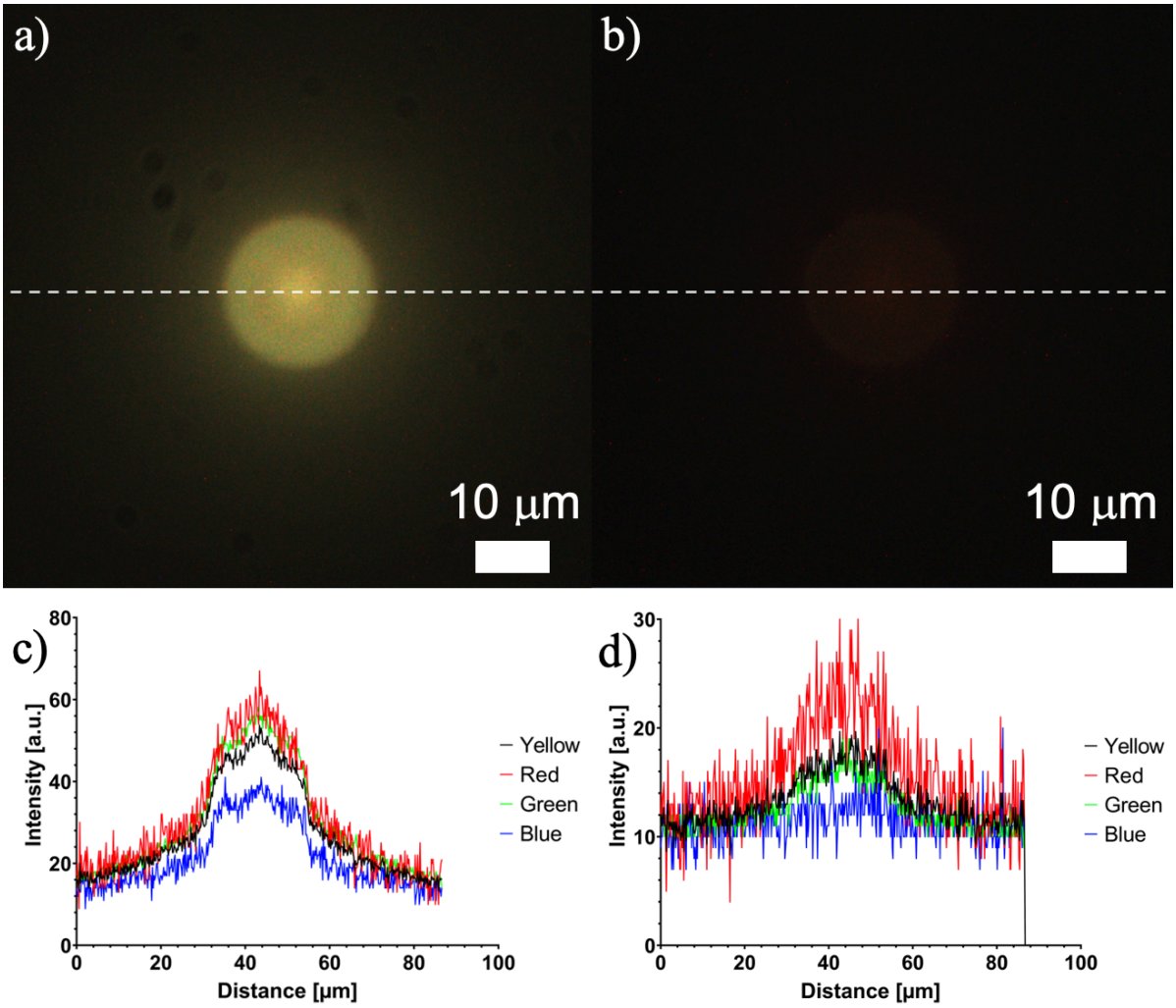

Figure 6.11: Fluorescence responses of loaded (a) and unloaded (b) pillars, together with their corresponding intensity plots (c and d, respectively) measured at the dotted line.

6.3.3. Mechanical analysis

After confirming the incorporation of the NDs inside the pillars, their effect on the Young's modulus of the resin was measured. Figure 6.12 shows the force-displacement plots from compression tests for loaded (a) and unloaded (b) pillars, performed by utilizing the Femtotools setup. The dissimilarities between different measurements were small, as all lines approximately followed the same trend during the loading and unloading phases of the test (indicated by the arrows).

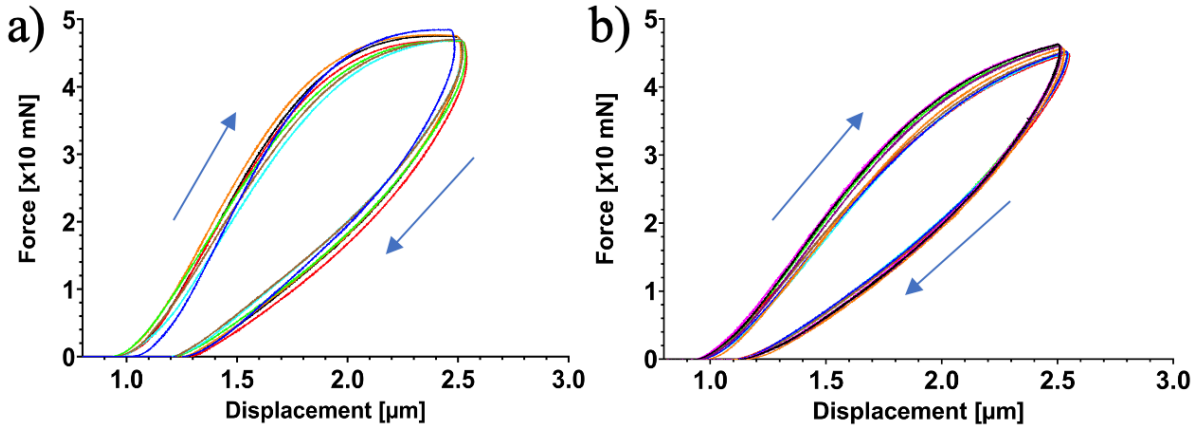

Figure 6.12: Force-displacement curves for loaded (a) and unloaded (b) pillars from compression tests.

The obtained data were in accordance with typical stress-strain curves for polymers (a) as shown in Figure 6.13. Three zones were distinguished from the measurement data (b) after comparison to the stress-strain, this being the initialization phase, the elastic range and the plastic range. At the initialization phase, the probe started compressing the pillar at approximately 1 microns of displacement. Due to surface irregularities, the force slowly builds up in the first phase. Hereafter, the elastic deformation range started with a linear slope until the yield limit is reached. After reaching the yield limit, the plastic deformation range started. The compression of the pillars was stopped after approximately 1.5 microns to not destroy the pillars. Lastly, the force was slowly released to return the probe back to its original location.

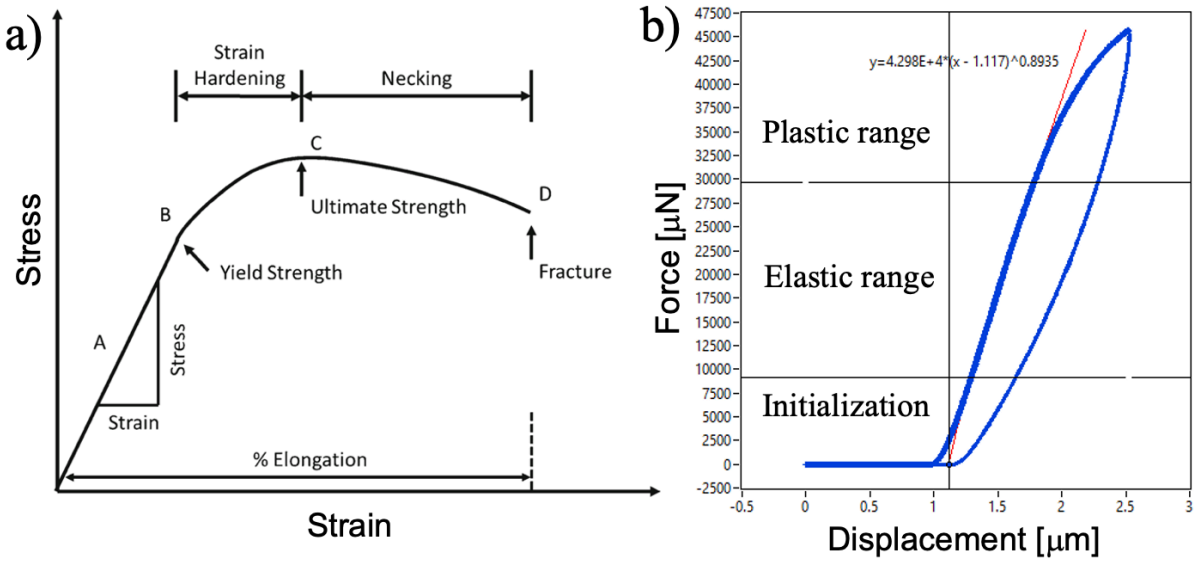

Figure 6.13: Typical stress-strain curve for polymers (a) [62], and an obtained force-displacement (b) curve from compression tests.

The stiffness of the pillars was determined through the *Femtotools Suite* software using the slope at the elastic range. As the dimensions of the structures was known, the Young's modulus was calculated through the stiffness. The box plots in Figure 6.14 show the results for the Young's modulus for the loaded and unloaded pillars. An average Young's modulus of 3.2 ± 0.22 GPa and 2.4 ± 0.10 GPa was calculated for the loaded and unloaded pillars, respectively. Thus, an increase of 33% for the Young's modulus was obtained for the loaded pillars as compared to unloaded ones.

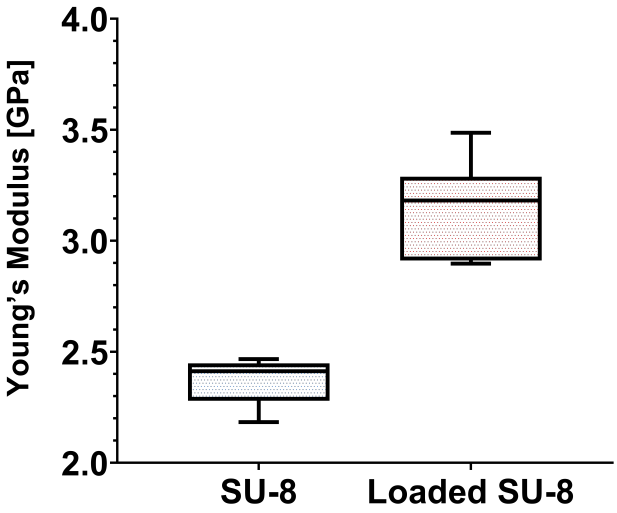

Figure 6.14: Box plots with the calculated Young's moduli of the loaded and unloaded pillars.

This increase in Young's modulus for ND loaded epoxy resins was also noticed by previous research [63, 64]. Mochalin and colleagues [63] report an increase in Young's modulus of 1000% for the epoxy resin Epon828 with a ND concentration of 7 wt.%. This increase in Young's modulus was attributed to the grafting of the amine functionalized NDs to the polymer resin through covalent bonding. This grafting of the NDs was confirmed by the same group [63], owing to the existence of amide bonds in the composite through Fourier-transform infrared spectroscopy (i.e., FTIR) analysis. Therefore, further analysis through FTIR or similar techniques may provide more insight for the recorded increase of Young's modulus for the manufactured loaded resin.

7

Conclusion

To enrich the limited available diamond microfabrication methods, a reproducible bottom-up method for the production of arbitrary 3D diamond loaded photoresist structures using 2PP has been developed. For this purpose, ND loaded SU-8 photoresist composites were formulated first by either mixing dry ND powders with SU-8 2007 or an acetone based diamond nanofluid with SU-8 2075. Best dispersion of diamond NPs was obtained with the diamond nanofluid. Characterization of the loaded resin (0.5 wt.% and 1 wt.%) through DLS measurements hinted to a monodispersed suspension with a narrow hydrodynamic size distribution around 20 nm. Spin coating the loaded resin resulted in smaller layer thicknesses in comparison to the base photoresist resin, likely as a result of the change in dynamic viscosity and liquid density. Furthermore, the fluorescence response caused by embedded diamond NPs also indicated a homogenous dispersion of NDs inside spin coated layers of loaded resin.

Optimization of the 2PP process employed on the loaded resin (1 wt.% ND) for the fabrication of micropillar arrays with a diameter and height of 20 microns resulted in optimal parameters of 7 mW (14%) laser power coupled with a scan speed of 0.2 mm/s. For this combination of laser power and scan speed, the optimal slicing and hatching distances were 0.3 μm and 0.2 μm, respectively. Using these optimized settings, 3D microstructures with feature sizes of 2 μm and aspect ratios of 1:5 were obtained.

To compare the properties of the ND loaded and unloaded base resins, micropillar arrays of both resins were successfully fabricated using the optimized 2PP parameters. Morphological characterization of the loaded and unloaded microstructures showed no significant differences aside through SEM analysis. WLI analysis indicated a maximum peak to valley roughness of approximately 300 nm and 700 nm on a pillar width of 20 μm for the loaded and the unloaded microstructures, respectively. Moreover, homogenous fluorescence response from the loaded pillars revealed successful incorporation of the NDs inside the structures after 2PP. Mechanical characterization by compression tests showed an average of 33% increase in Young's modulus for the loaded micropillars in comparison to unloaded micropillars (i.e., 3.2 ± 0.22 GPa and 2.4 ± 0.10 GPa, respectively).

8

Recommendations for future work

After the successful fabrication of diamond loaded pillars, subsequent studies pursuing the development and implementation of the newly proposed production method of glassy carbon and diamond core-shell microstructures could be employed. Aiming at better understanding and possible improvement of the achieved results, research can be conducted on the various production steps. These steps include preparation of the loaded resin, 2PP, subsequent pyrolysis and CVD growth steps, as well as the characterization of resin and different microstructured materials. In sum, the recommendations for future research are:

- There should be research conducted to better understand the behavior of NDs inside the photoresist. Hereby, the characterization can be redone with varying ND percentage. In such, the effect of different quantities of NDs on the fluorescence response, bubble formation, printability and mechanical strength can be explored and optimized.
- To improve the microstructures in terms of structural integrity, an attempt could be made to reduce the air bubbles in the resin by filtering the resin through a syringe filter. Reducing the amount of bubbles might also lead to an even larger increase in the mechanical strength of the microstructures created with the loaded resin.
- The reliability of the morphological characterization of the microstructures can be improved by adding a thin layer of conductive metal layer, such as gold. By improving the reflection on the surfaces with gold, better estimates for roughness and topology of the microstructures can be obtained through WLI. Furthermore, the added conductivity decreases the problem of charge accumulation during SEM characterization. This decrease might give a better view on the surface characteristics of the microstructures.
- Further compositional and microstructural characterization of the loaded resin should be conducted through a properly calibrated DLS system as described by Osawa [55]. Moreover, TEM analysis can be used to get more insight about the real size and distribution of the NDs instead of the hydrodynamic size as measured by DLS. Additionally, to get a total picture of the NP behavior, the covalent bonding of the NDs to the epoxy resin can be examined for possible grafting as mentioned by Mochalin and colleagues [63] through infrared spectroscopy.
- The resolution can possibly be increased by further optimizing the 2PP of structures with smaller feature sizes and higher aspect ratios. To decrease the print time for larger structures in the order of 20 microns, the 25x objective lens could be considered. Furthermore, a shift towards the fabrication of complex 3D microstructures could be examined, which might exploit the full potential of the 2PP process.
- When the diamond loaded structures are obtained, the next steps of the overarching project can be conducted. Carbonizing the diamond loaded microstructures through pyrolysis will lead to the formation of glassy carbon templates [45]. Afterwards, diamond films could be coated on the microstructures by CVD through the added strength and resistivity from the transition from polymer to glassy carbon.
- Finally, the application of glassy carbon and diamond core-shell structures can be explored in the fields of MEMS, micro-devices and sensors. The combination of diamond with C-MEMS

might open possibilities for battery miniaturization problems [40]. Furthermore, elemental doping with boron during the CVD process can lead to 3D complex BDD microelectrodes with improved efficiency due to their high surface-to-volume ratios. The increased surface area of complex interconnected BDD electrodes opens possibilities for a plethora of applications ranging from biosensors to supercapacitors [38, 39, 40, 41, 42].

A

Solvent test

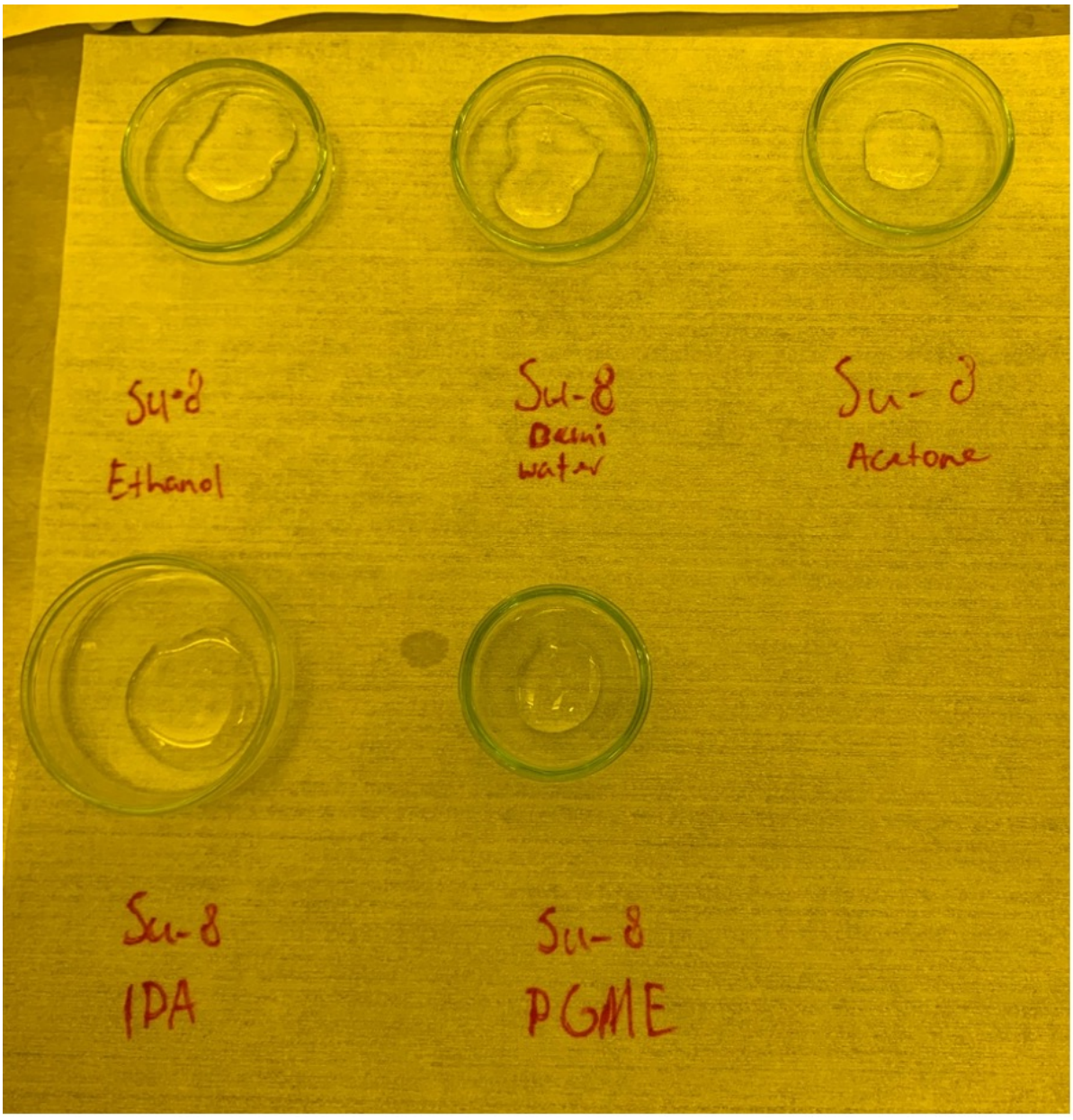

Figure A.1: Solvent test with SU-8 2007 before adding the solvents ethanol, water, acetone, isopropyl alcohol (IPA) and propylene glycol methyl ether (PGME) to their respective places.

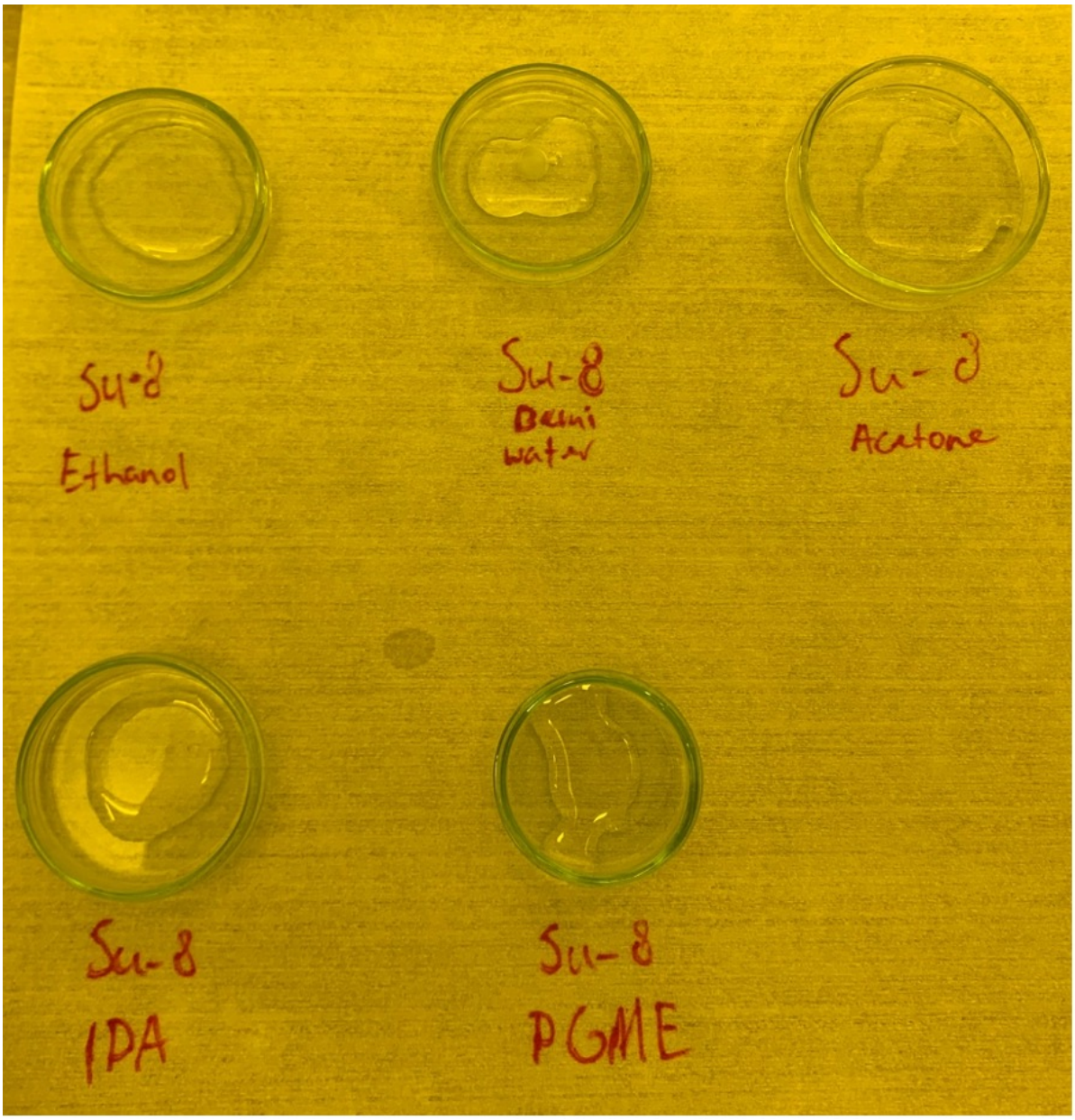

Figure A.2: Result of the solvent test 30 minutes after adding one droplet of the indicated solvents. The acetone and PGME got completely dissolved in the SU-8 2007 resin. The ethanol and IPA were partly miscible, while the water was not miscible in SU-8 2007.

B

Dry powder resin

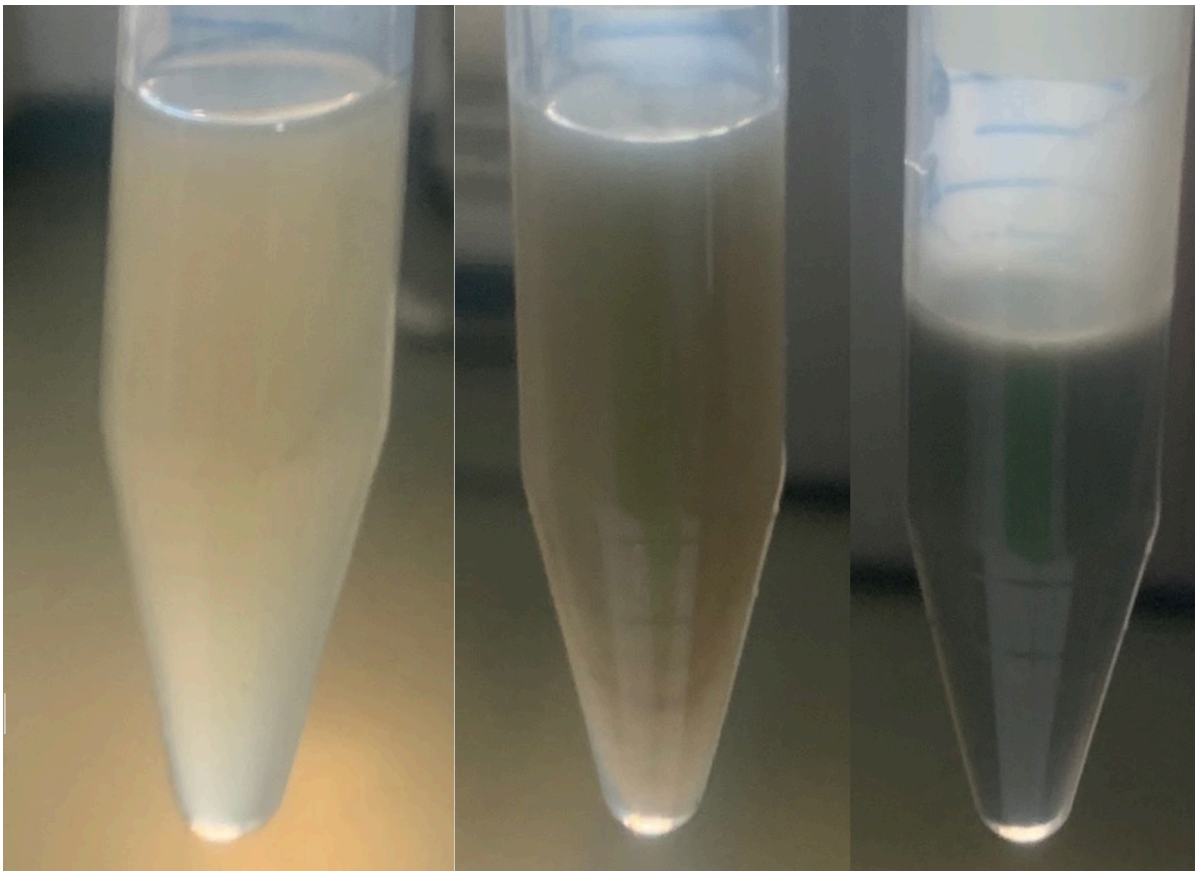

Figure B.1: Loaded resin created by suspending dry ND powder (uDiamond Molto, Carbodeon) and SU-8 2007. The total ND concentration on the fluid is 0.1, 0.25 and 1 wt.% from left to right, respectively.

Figure B.2: Partly sedimented loaded SU-8 2007 (0.25 wt.%), one day after preparation.

C

Air bubbles

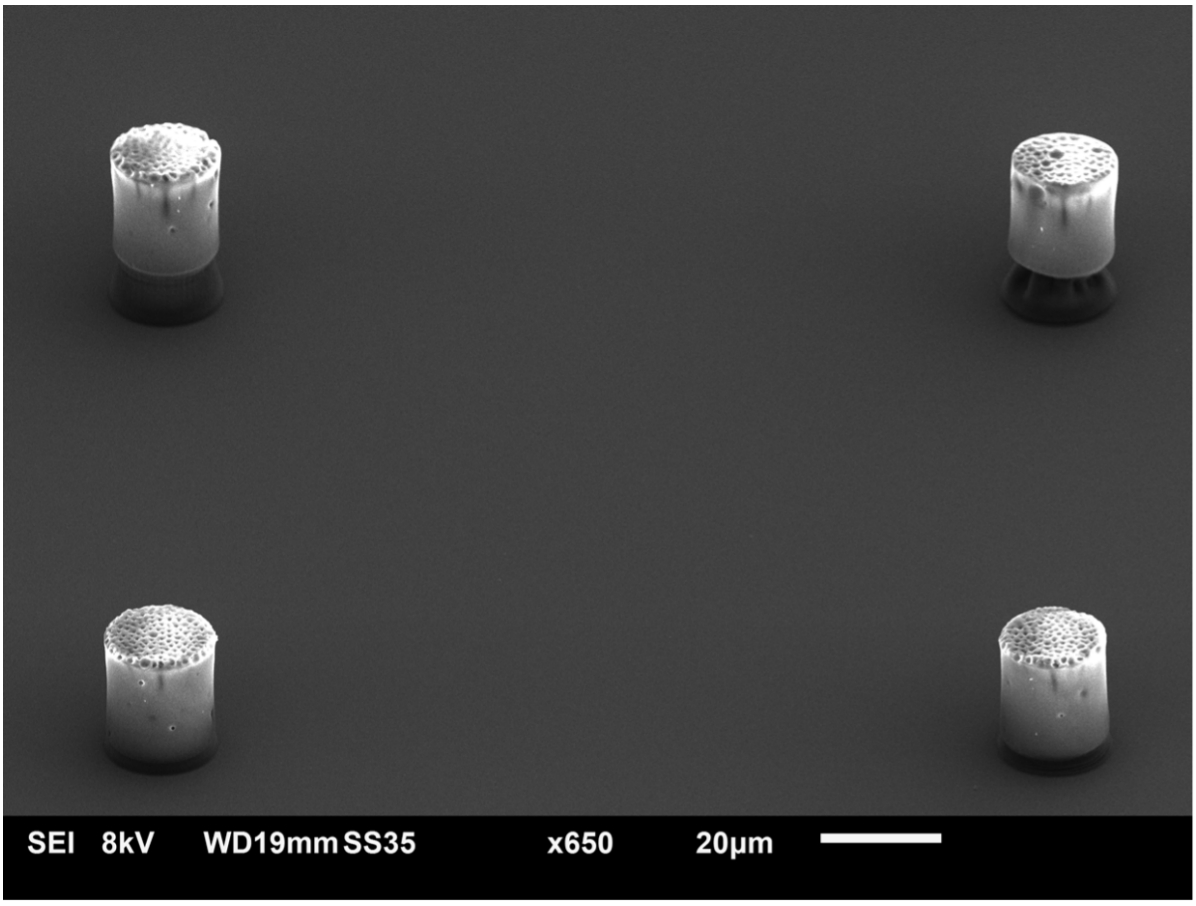

Figure C.1: SEM images of partly destroyed pillar arrays, due to entrapped air bubbles.

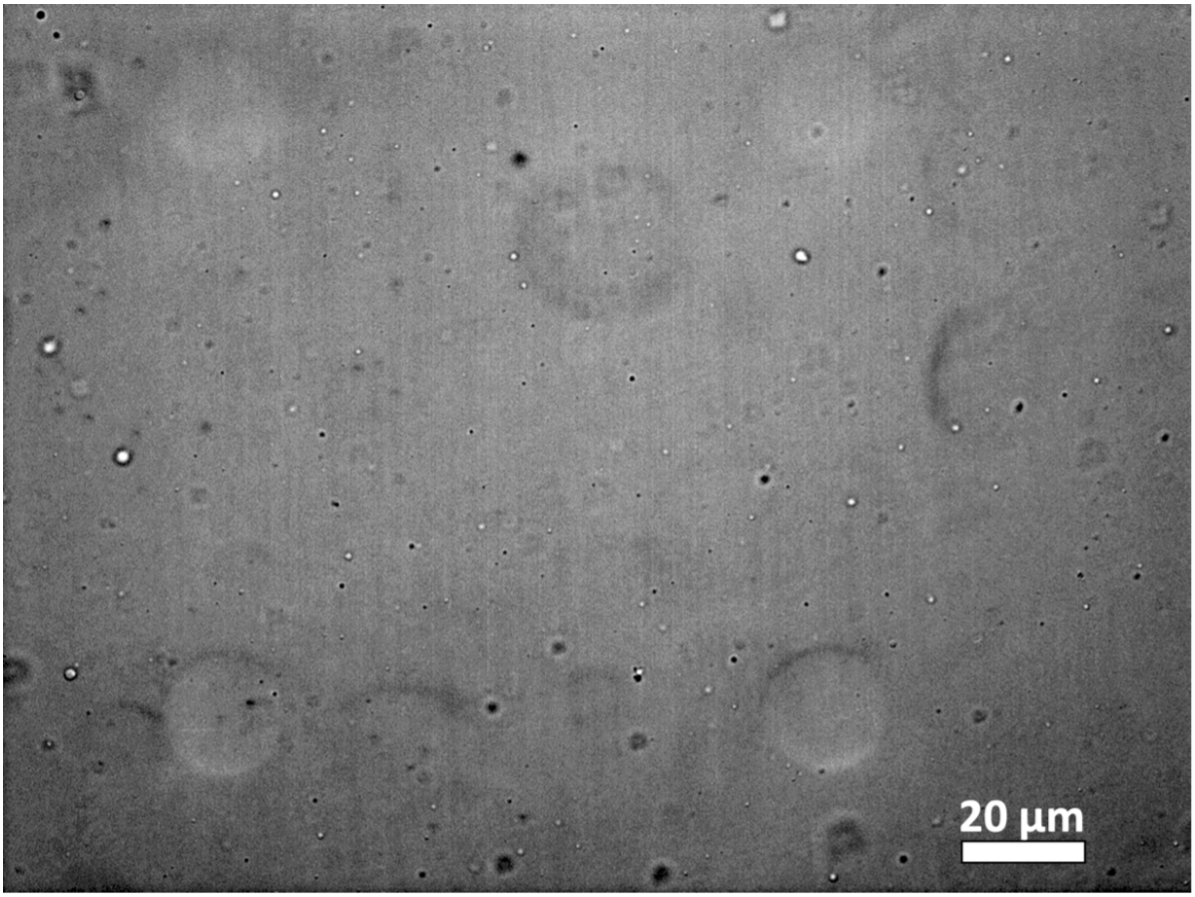

Figure C.2: Optical image through the NanoScribe camera during the print of a pillar array. The dark and white spots are the entrapped air bubbles, distributed randomly in size and location throughout the substrate.

D

Resins and nanofluid for dynamic light scattering

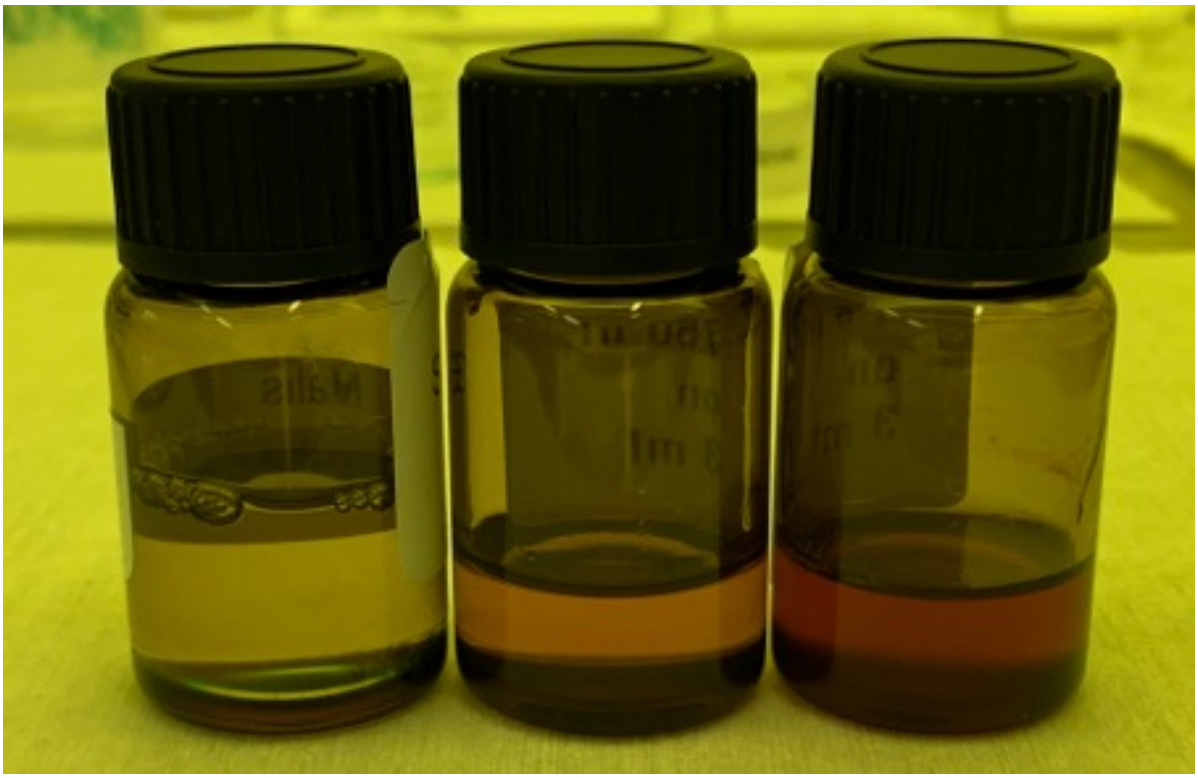

Figure D.1: Optical image of SU-8 2075, ND loaded SU-8 2075 with 0.5 wt.% and 1 wt.% from left to right, respectively.

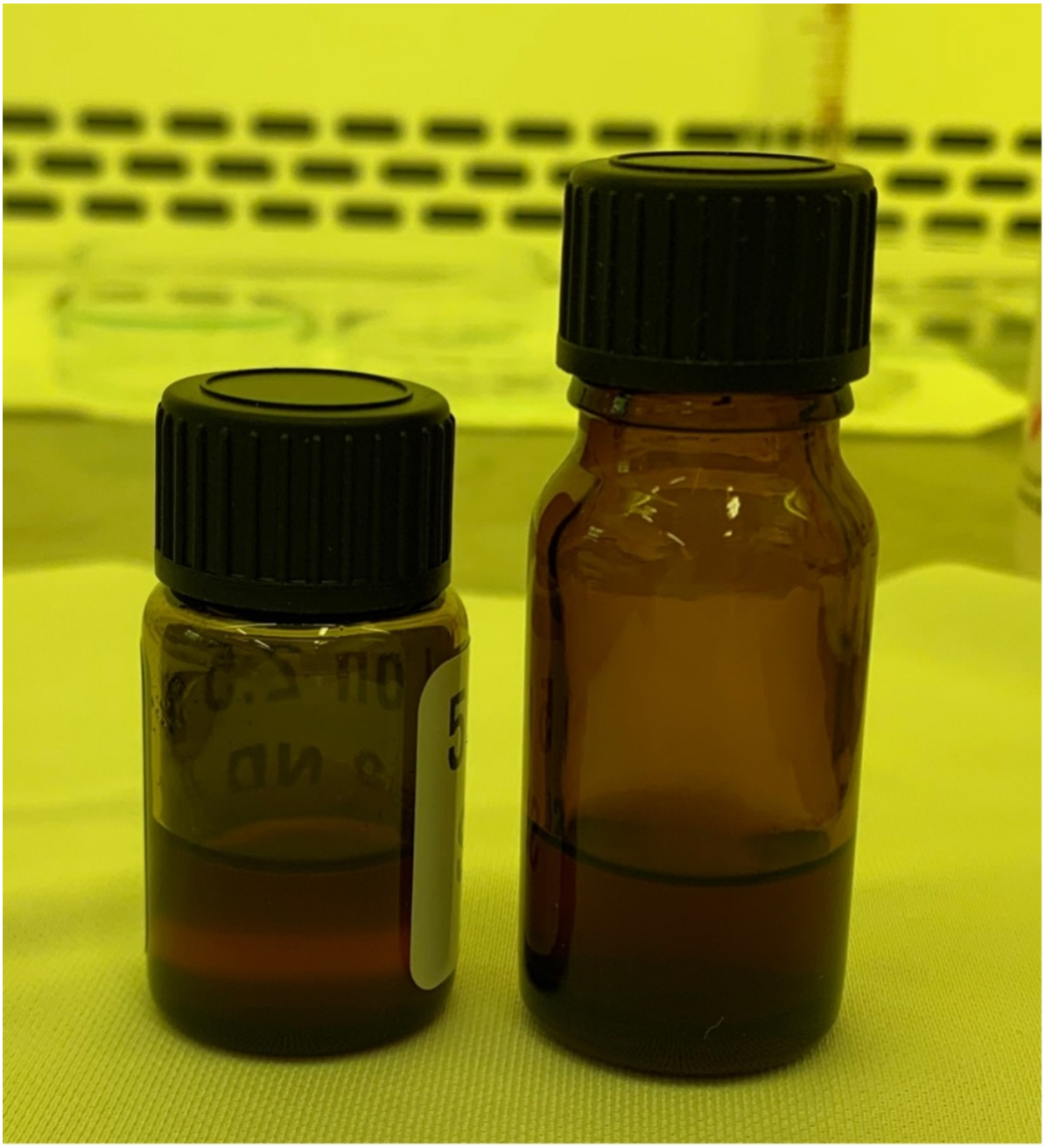

Figure D.2: Optical image of ND loaded SU-8 2075 (left) and the nanofluid RT-Ac-4 (right).

E

3D structures

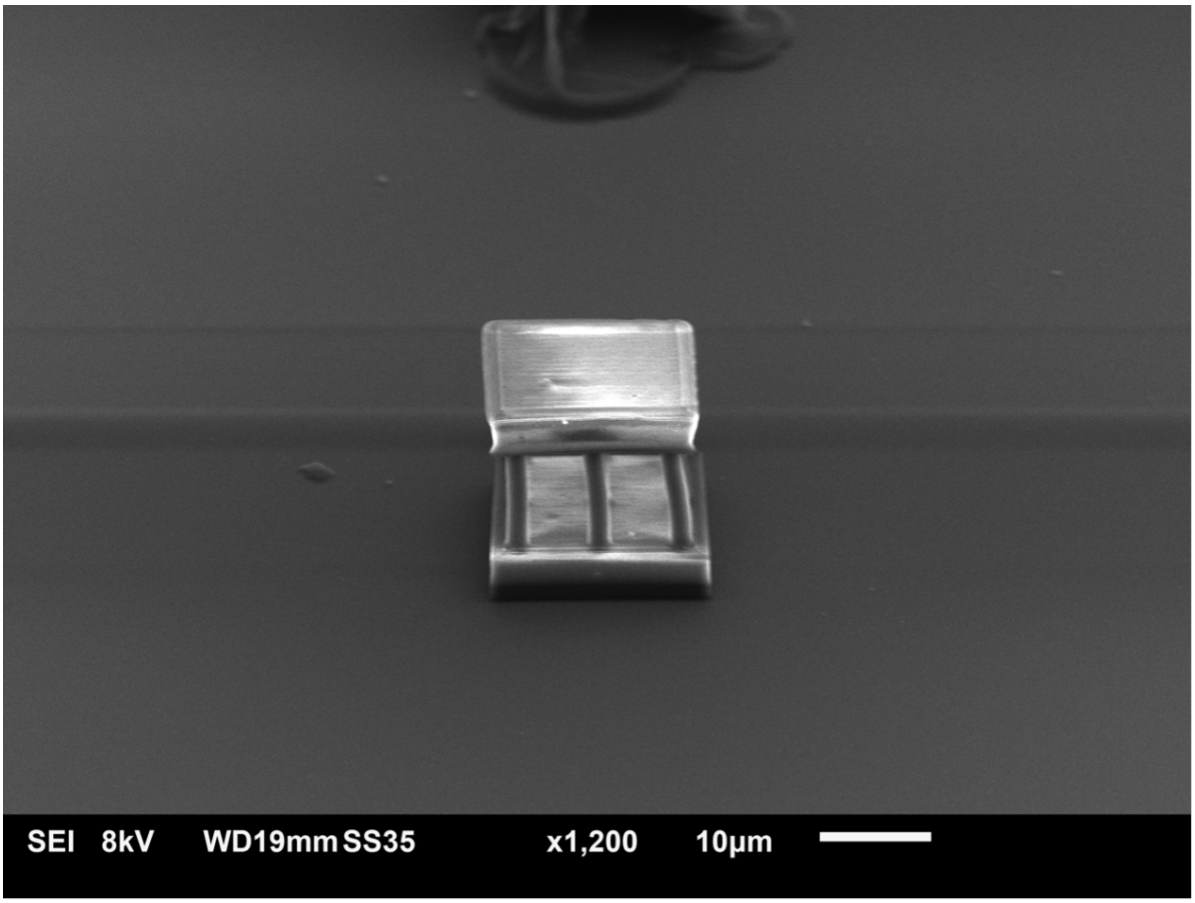

Figure E.1: SEM image of a 3D structure with struts of 2 microns in diameter and 10 microns in height (1:5 aspect ratio), printed using the loaded resin created from the nanofluid and optimized parameters.

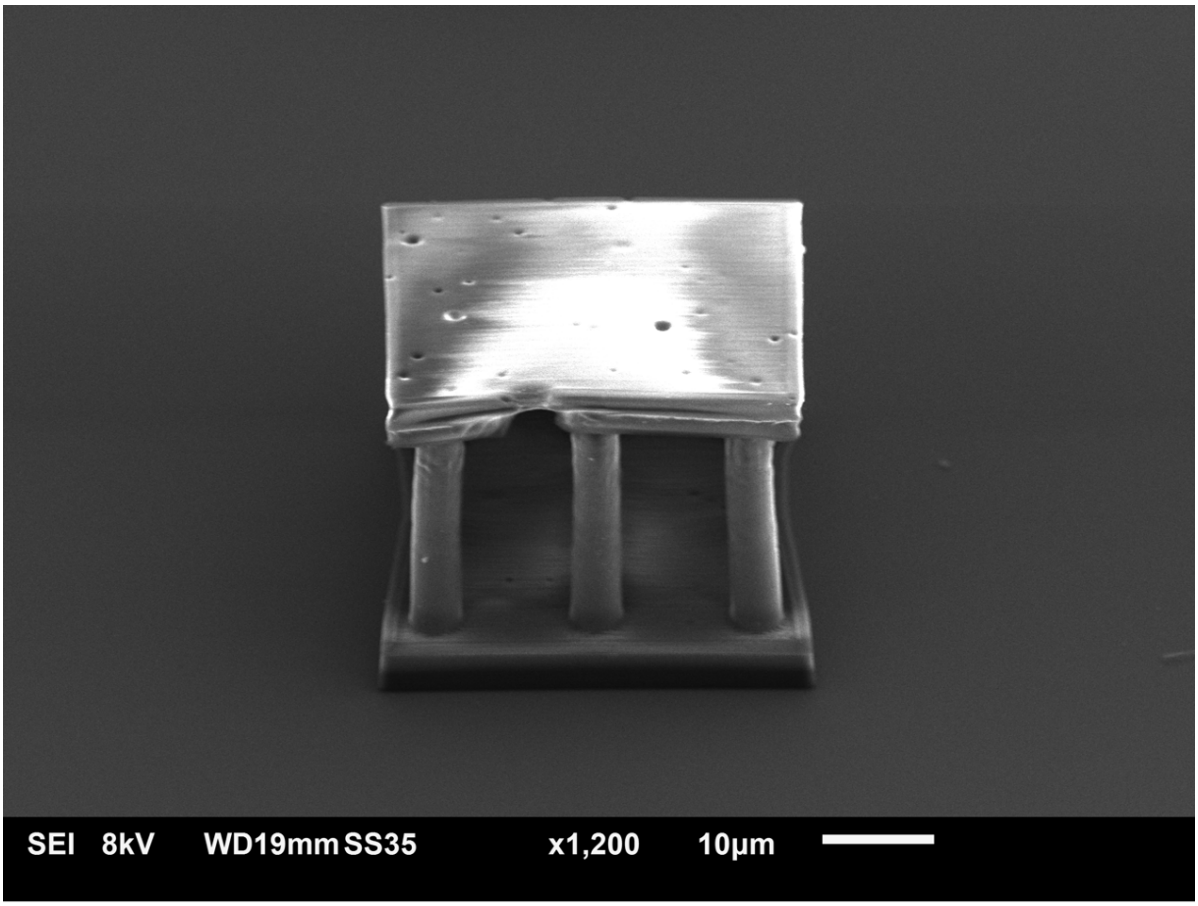

Figure E.2: SEM image of a 3D structure with struts of 5 microns in diameter and 20 microns in height (1:4 aspect ratio), printed using the loaded resin created from the nanofluid and optimized parameters.

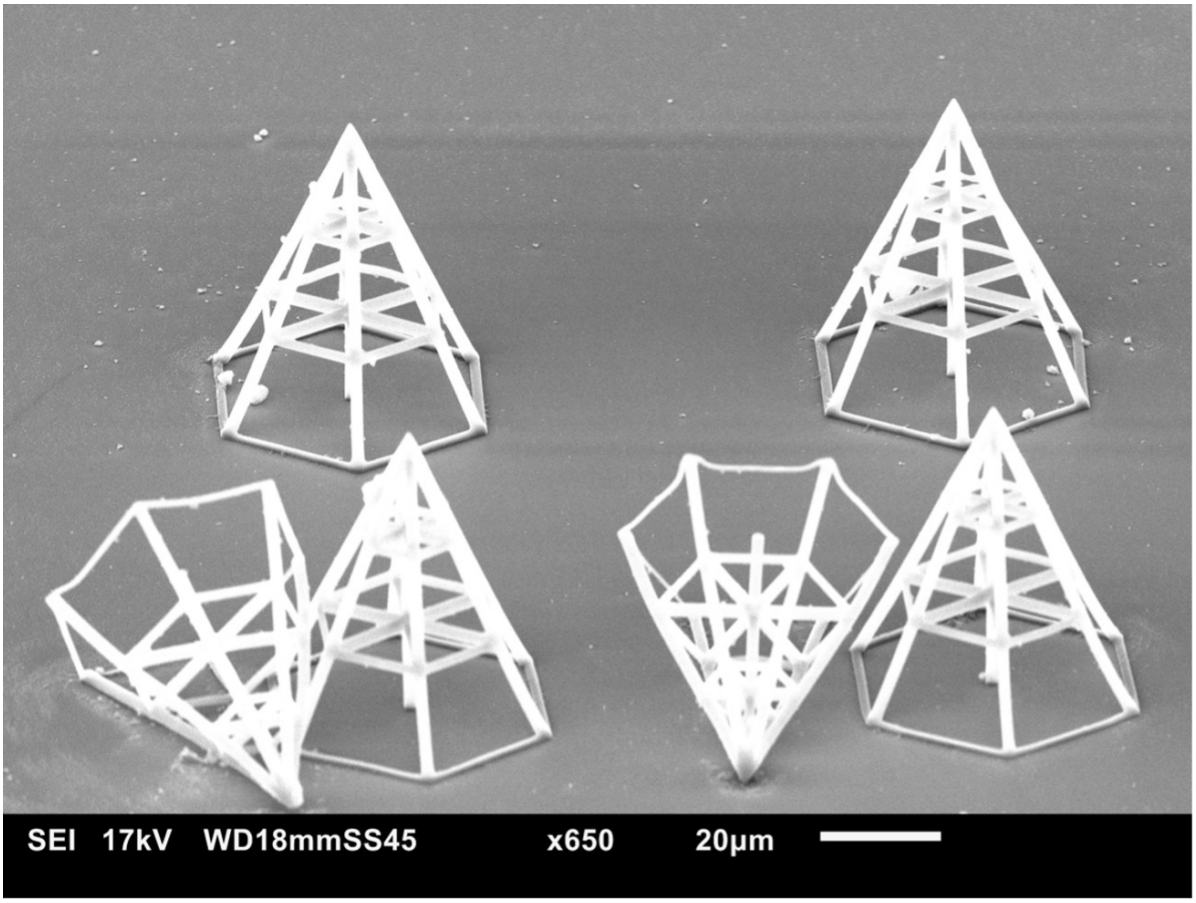

Figure E.3: SEM image of pyramid-like structures composed of 2-micron struts, fabricated out of loaded resist formulated from dry powder. The structures delaminate due to the limited substrate interface.

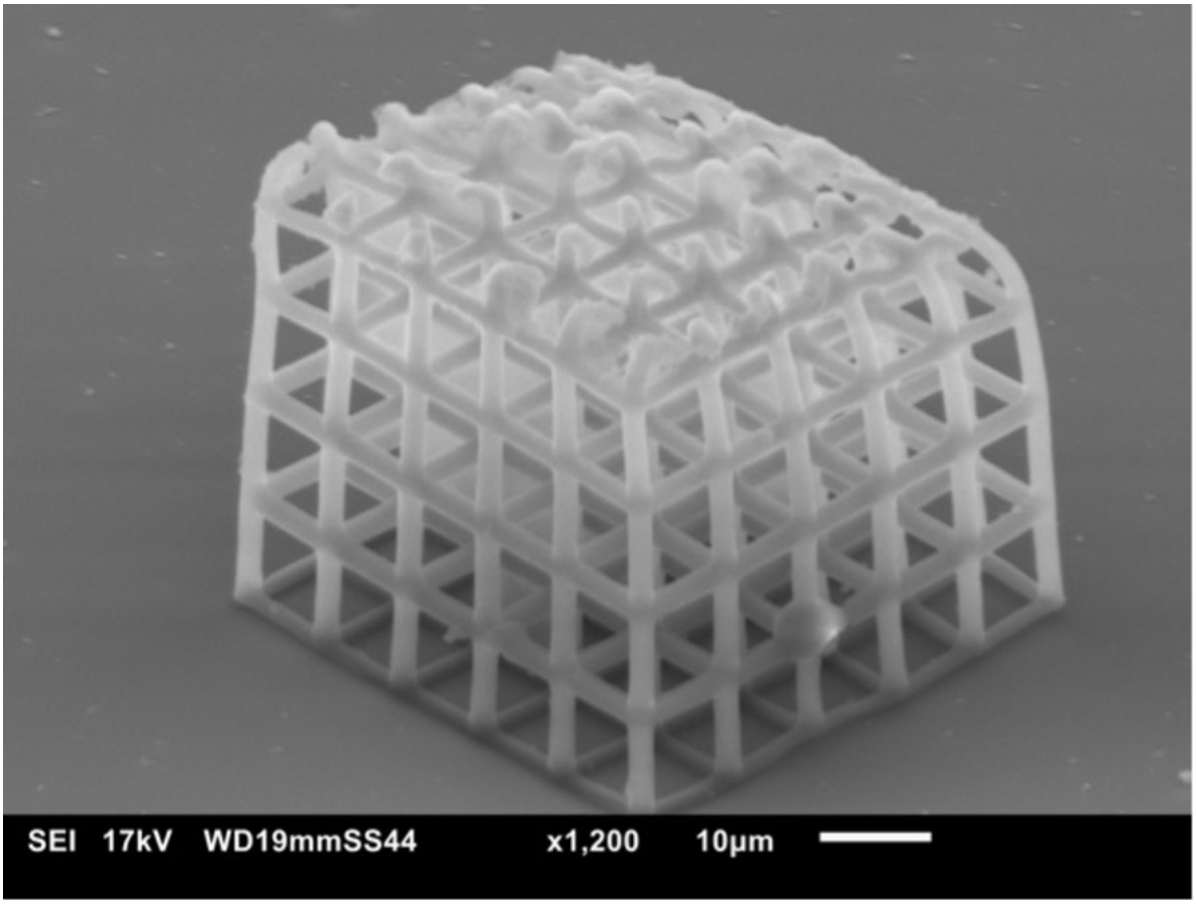

Figure E.4: SEM image of a 3D scaffold composed of struts with 2 microns of diameter and 10 microns of length, fabricated out of loaded resist formulated from dry powder.

Bibliography

[1] Anirudha V. Sumant et al. “Ultrananocrystalline and Nanocrystalline Diamond Thin Films for MEMS/NEMS Applications”. In: *MRS Bulletin* 35.4 (2010), pp. 281–288. DOI: 10.1557/mrs2010.550.

[2] Orlando Auciello and Dean M. Aslam. “Review on advances in microcrystalline, nanocrystalline and ultrananocrystalline diamond films-based micro/nano-electromechanical systems technologies”. In: *Journal of Materials Science* 56.12 (2021), pp. 7171–7230. DOI: 10.1007/s10853-020-05699-9.

[3] Kazuhisa Miyoshi. In: *Structures and mechanical properties of natural and synthetic diamonds (Chapter 8)*. National Aeronautics and Space Administration, Lewis Research Center, 1998.

[4] Sergey V. Kidalov and Fedor M. Shakhov. “Thermal Conductivity of Diamond Composites”. In: *Materials* 2.4 (2009), pp. 2467–2495. DOI: 10.3390/ma2042467.

[5] M. Rodrigo et al. “Oxidation of 4-chlorophenol at boron-doped diamond electrode for wastewater treatment”. In: *Journal of The Electrochemical Society* 148 (2001). DOI: 10.1149/1.1362545.

[6] J. Iniesta et al. “Electrochemical oxidation of 3-methylpyridine at a boron-doped diamond electrode: application to electroorganic synthesis and wastewater treatment”. In: *Electrochemistry Communications* 3.7 (2001), pp. 346–351. DOI: 10.1016/S1388-2481(01)00174-6.

[7] M. Mahrokh, Hongyu Yu, and Yuejin Guo. “Thermal Modeling of GaN HEMT Devices With Diamond Heat-Spreader”. In: *IEEE Journal of the Electron Devices Society* 8 (2020), pp. 986–991. DOI: 10.1109/JEDS.2020.3023081.

[8] André F. Sartori et al. “Inkjet-Printed High-Q Nanocrystalline Diamond Resonators”. In: *Small* 15.4 (2019), p. 1803774. DOI: https://doi.org/10.1002/smll.201803774.

[9] Michael W. Varney et al. “Polycrystalline-Diamond MEMS Biosensors Including Neural Microelectrode-Arrays”. In: *Biosensors* 1.3 (2011), pp. 118–133. DOI: 10.3390/bios1030118.

[10] X Ding et al. “Fabrication of a micro-size diamond tool using a focused ion beam”. In: *Journal of Micromechanics and Microengineering* 18.7 (2008), p. 075017. DOI: 10.1088/0960-1317/18/7/075017.

[11] G.F. Ding et al. “Micromachining of CVD diamond by RIE for MEMS applications”. In: *Diamond and Related Materials* 14.9 (2005), pp. 1543–1548. DOI: 10.1016/j.diamond.2005.04.011.

[12] A.R. Krauss et al. “Ultrananocrystalline diamond thin films for MEMS and moving mechanical assembly devices”. In: *Diamond and Related Materials* 10.11 (2001), pp. 1952–1961. DOI: 10.1016/S0925-9635(01)00385-5.

[13] André F. Sartori et al. “Template-assisted bottom-up growth of nanocrystalline diamond micropillar arrays”. In: *Diamond and Related Materials* 95 (2019), pp. 20–27. DOI: 10.1016/j.diamond.2019.03.017.

[14] Stepan Linnik, Vitalii Okhotnikov, and Alexander Gaydaychuk. “Deposition and Patterning of Polycrystalline Diamond Films Using Traditional Photolithography and Reactive Ion Etching”. In: *Coatings* 7.9 (2017). DOI: 10.3390/coatings7090148.

[15] Floyd Versluis. “Bottom-up manufacturing of nanocrystalline diamond micro structures and components”. MA thesis. TU Delft, 2020.

[16] Vitalii Okhotnikov et al. “Selective deposition of polycrystalline diamond films using photolithography with addition of nanodiamonds as nucleation centers”. In: *IOP Conference Series: Materials Science and Engineering* 116 (Feb. 2016), p. 012001. DOI: 10.1088/1757-899X/116/1/012001.

[17] Satoshi Katsumata, Yoshimichi Oobuchi, and Tanemasa Asano. “Patterning of CVD diamond films by seeding and their field emission properties”. In: *Diamond and Related Materials* 3.11 (1994), pp. 1296–1300. DOI: 10.1016/0925-9635(94)90141-4.

[18] Bidhan Pramanick et al. “Effect of pyrolysis process parameters on electrical, physical, chemical and electro-chemical properties of SU-8-derived carbon structures fabricated using the C-MEMS process”. In: *Materials Today: Proceedings* 5.3, Part 3 (2018). International Conference on Functional Nano-Materials, 28-29 September, 2016, pp. 9669–9682. DOI: 10.1016/j.matpr.2017.10.153.

[19] Andrey Vyatskikh et al. “Additive manufacturing of 3D nano-architected metals”. In: *Nature Communications* 9.1 (2018), p. 593. DOI: 10.1038/s41467-018-03071-9.

[20] J. C. Arnault. “Nanodiamonds: From Synthesis and Purification to Deposition Techniques, Hybrids Fabrication and Applications”. In: *Carbon Nanoparticles and Nanostructures*. Ed. by Nianjun Yang, Xin Jiang, and Dai-Wen Pang. Cham: Springer International Publishing, 2016, pp. 1–45. ISBN: 978-3-319-28782-9. DOI: 10.1007/978-3-319-28782-9_1.

[21] Chunlei Wang et al. “A novel method for the fabrication of high-aspect ratio C-MEMS structures”. In: *Journal of Microelectromechanical Systems* 14.2 (2005), pp. 348–358. DOI: 10.1109/JMEMS.2004.839312.

[22] J. M. T. Thompson and Paul W. May. “Diamond thin films: a 21st-century material”. In: *Philosophical Transactions of the Royal Society of London. Series A: Mathematical, Physical and Engineering Sciences* 358.1766 (2000), pp. 473–495. DOI: 10.1098/rsta.2000.0542.

[23] E.M.A. Fuentes-Fernandez et al. “Synthesis and characterization of microcrystalline diamond to ultrananocrystalline diamond films via Hot Filament Chemical Vapor Deposition for scaling to large area applications”. In: *Thin Solid Films* 603 (2016), pp. 62–68. DOI: 10.1016/j.tsf.2015.11.088.

[24] Ivan Rehor and Petr Cigler. “Precise estimation of HPHT nanodiamond size distribution based on transmission electron microscopy image analysis”. In: *Diamond and Related Materials* 46 (2014), pp. 21–24. DOI: 10.1016/j.diamond.2014.04.002.

[25] V. Pichot et al. “Detonation of nanosized explosive: New mechanistic model for nanodiamond formation”. In: *Diamond and Related Materials* 54 (2015). Advances in Diamond Thin Films and Novel Nanocarbon Materials, pp. 59–63. DOI: 10.1016/j.diamond.2014.09.013.

[26] David Amans et al. “Nanodiamond synthesis by pulsed laser ablation in liquids”. In: *Diamond and Related Materials* 18.2 (2009). NDNC 2008 Proceedings of the International Conference on New Diamond and Nano Carbons 2008, pp. 177–180. DOI: 10.1016/j.diamond.2008.10.035.

[27] Boris Zousman and Olga Levinson. “Monodispersed Nanodiamonds Produced by Laser Ablation”. In: *MRS Online Proceedings Library* 1452.1 (2012), pp. 32–38. DOI: 10.1557/opl.2012.1339.

[28] Boris Kharisov, Oxana Kharissova, and Leonardo Chávez-Guerrero. “Synthesis Techniques, Properties, and Applications of Nanodiamonds”. In: *Synthesis and Reactivity in Inorganic Metal-organic and Nano-metal Chemistry - SYNTH REACT INORG MET-ORG NAN* 40 (2010), pp. 84–101. DOI: 10.3109/10799890903555665.

[29] Xiangyang Xu et al. “Effect of sodium oleate adsorption on the colloidal stability and zeta potential of detonation synthesized diamond particles in aqueous solutions”. In: *Diamond and Related Materials* 14.2 (2005), pp. 206–212. DOI: 10.1016/j.diamond.2004.11.004.

[30] Jean-Paul Boudou et al. “High yield fabrication of fluorescent nanodiamonds”. In: *Nanotechnology* 20.23 (2009), p. 235602. DOI: 10.1088/0957-4484/20/23/235602.

[31] Pooria Karami et al. “Polymer/nanodiamond composites - a comprehensive review from synthesis and fabrication to properties and applications”. In: *Advances in Colloid and Interface Science* 269 (2019), pp. 122–151. DOI: 10.1016/j.cis.2019.04.006.

[32] M.R. Ayatollahi et al. “Tribological and mechanical properties of low content nanodiamond/epoxy nanocomposites”. In: *Composites Part B: Engineering* 43.8 (2012), pp. 3425–3430. ISSN: 1359-8368. DOI: https://doi.org/10.1016/j.compositesb.2012.01.022.

[33] S.M. Kong, M. Mariatti, and J.J.C. Busfield. “Effects of types of fillers and filler loading on the properties of silicone rubber composites”. In: *Journal of Reinforced Plastics and Composites* 30.13 (2011), pp. 1087–1096. DOI: 10.1177/0731684411416267.

[34] Seira Morimune-Moriya and Takashi Nishino. “Strong, tough, transparent and highly heat-resistant acrylic glass based on nanodiamond”. In: *Polymer* 222 (2021), p. 123661. DOI: 10.1016/j.polymer.2021.123661.

[35] Valeriy V. Karbushev et al. “Preparation of Polymer-Nanodiamond Composites with Improved Properties”. In: *1st International Conference On New Materials for Extreme Environment*. Vol. 59. Advanced Materials Research. Trans Tech Publications Ltd, 2009, pp. 275–278. DOI: 10.4028/www.scientific.net/AMR.59.275.

[36] Julian Taurozzi, Vincent Hackley, and Mark Wiesner. *Preparation of Nanoparticle Dispersions from Powdered Material Using Ultrasonic Disruption*. 2012. DOI: 10.6028/NIST.SP.1200-2.

[37] Xiaoqin Zhou, Yihong Hou, and Jieqiong Lin. “A review on the processing accuracy of two-photon polymerization”. In: *AIP Advances* 5.3 (2015), p. 030701. DOI: 10.1063/1.4916886.

[38] Yasuaki Einaga, John S. Foord, and Greg M. Swain. “Diamond electrodes: Diversity and maturity”. In: *MRS Bulletin* 39.6 (2014), pp. 525–532. DOI: 10.1557/mrs.2014.94.

[39] Fang Gao and Christoph E. Nebel. “Diamond-Based Supercapacitors: Realization and Properties”. In: *ACS Applied Materials & Interfaces* 8.42 (2016), pp. 28244–28254. DOI: 10.1021/acsami.5b07027.

[40] Chunlei Wang et al. “C-MEMS for the Manufacture of 3D Microbatteries”. In: *Electrochemical and Solid-State Letters* 7.11 (2004), A435. DOI: 10.1149/1.1798151.

[41] Biuck Habibi and Mojtaba Jahanbakhshi. “A glassy carbon electrode modified with carboxylated diamond nanoparticles for differential pulse voltammetric simultaneous determination of guanine and adenine”. In: *Microchimica Acta* 183.7 (2016), pp. 2317–2325. DOI: 10.1007/s00604-016-1868-6.

[42] Takeshi Kondo et al. “Porous boron-doped diamond electrodes fabricated via two-step thermal treatment”. In: *Carbon* 77 (2014), pp. 783–789. DOI: 10.1016/j.carbon.2014.05.082.

[43] Zhe Xing et al. “Biological Effects of Functionalizing Copolymer Scaffolds with Nanodiamond Particles”. In: *Tissue Engineering Part A* 19.15-16 (2013). PMID: 23574424, pp. 1783–1791. DOI: 10.1089/ten.tea.2012.0336.

[44] João Nunes-Pereira et al. “Antimicrobial and Antibiofilm Properties of Fluorinated Polymers with Embedded Functionalized Nanodiamonds”. In: *ACS Applied Polymer Materials* 2.11 (2020), pp. 5014–5024. DOI: 10.1021/acsapm.0c00869.

[45] Braulio Cardenas-Benitez et al. “Pyrolysis-induced shrinking of three-dimensional structures fabricated by two-photon polymerization: experiment and theoretical model”. In: *Microsystems & Nanoengineering* 5.1 (2019), p. 38. DOI: 10.1038/s41378-019-0079-9.

[46] R. Bogdanowicz et al. “Amperometric sensing of chemical oxygen demand at glassy carbon and silicon electrodes modified with boron-doped diamond”. In: *Sensors and Actuators B: Chemical* 189 (2013). Selected Papers from the 26th European Conference on Solid-State Transducers, pp. 30–36. DOI: 10.1016/j.snb.2012.12.007.

[47] *Carbodeon Ltd. Oy. Finland.* http://www.carbodeon.net/. Retrieved August 13, 2021.

[48] *Ray Techniques Ltd. Israel.* https://www.nanodiamond.co.il/. Retrieved August 13, 2021.

[49] Henry E. Williams et al. “Order of multiphoton excitation of sulfonium photo-acid generators used in photoresists based on SU-8”. In: *Journal of Applied Physics* 121.22 (2017), p. 223104. DOI: 10.1063/1.4984828.

[50] Cyrus Weijie Beh, Weizhuang Zhou, and Tza-Huei Wang. “PDMS–glass bonding using grafted polymeric adhesive – alternative process flow for compatibility with patterned biological molecules”. In: *Lab Chip* 12 (20 2012), pp. 4120–4127. DOI: 10.1039/C2LC40315C.

[51] G. Wang et al. “Polymersomes as radionuclide carriers loaded via active ion transport through the hydrophobic bilayer”. In: *Soft Matter* 9 (3 2013), pp. 727–734. DOI: 10.1039/C2SM26434J.

[52] M. Loos et al. “The effect of acetone addition on the properties of epoxy”. In: *Polimeros-ciencia E Tecnologia* 18 (2008), pp. 76–80. DOI: 10.1590/s0104-14282008000100015.

[53] Vincent A. Hackley and Jeffrey D. Clogston. “Measuring the Hydrodynamic Size of Nanoparticles in Aqueous Media Using Batch-Mode Dynamic Light Scattering”. In: *Characterization of Nanoparticles Intended for Drug Delivery*. Ed. by Scott E. McNeil. Totowa, NJ: Humana Press, 2011, pp. 35–52. ISBN: 978-1-60327-198-1. DOI: 10.1007/978-1-60327-198-1_4.

[54] S. K. Mehta et al. “Effect of Cationic Surfactant Head Groups on Synthesis, Growth and Agglomeration Behavior of ZnS Nanoparticles”. In: *Nanoscale Research Letters* 4.10 (2009), p. 1197. DOI: 10.1007/s11671-009-9377-8.

[55] Eiji Osawa. “Remarks on the particle-size determination of nanoamando by dynamic light scattering”. In: *NCRI Technical Bulletin* 2 (2007).

[56] Jeff W Lichtman and José-Angel Conchello. “Fluorescence microscopy”. In: *Nature Methods* 2.12 (2005), pp. 910–919. DOI: 10.1038/nmeth817.

[57] Marco D. Torelli, Nicholas A. Nunn, and Olga A. Shenderova. “A Perspective on Fluorescent Nanodiamond Bioimaging”. In: *Small* 15.48 (2019), p. 1902151. DOI: 10.1002/smll.201902151.

[58] Gregoire Laporte and Demetri Psaltis. “STED imaging of green fluorescent nanodiamonds containing nitrogen-vacancy-nitrogen centers”. In: *Biomed. Opt. Express* 7.1 (2016), pp. 34–44. DOI: 10.1364/BOE.7.000034.

[59] Tse-Luen Wee et al. “Preparation and characterization of green fluorescent nanodiamonds for biological applications”. In: *Diamond and Related Materials* 18.2 (2009). NDNC 2008 Proceedings of the International Conference on New Diamond and Nano Carbons 2008, pp. 567–573. DOI: 10.1016/j.diamond.2008.08.012.

[60] Jan Jeske et al. “Stimulated emission from nitrogen-vacancy centres in diamond”. In: *Nature Communications* 8.1 (2017), p. 14000. DOI: 10.1038/ncomms14000.

[61] Rafał Walczak, P. Śniadek, and Jan Dziuban. “SU-8 photoresist as material of optical passive components integrated with analytical microsystems for real-time polymerase chain reaction”. In: *Optica Applicata* 41 (2011).

[62] Hanpin Lim and Stephen W. Hoag. “Plasticizer Effects on Physical–Mechanical Properties of Solvent Cast Soluplus®Films”. In: *AAPS PharmSciTech* 14.3 (2013), pp. 903–910. DOI: 10.1208/s12249-013-9971-z.

[63] Vadym N. Mochalin et al. “Covalent Incorporation of Aminated Nanodiamond into an Epoxy Polymer Network”. In: *ACS Nano* 5.9 (Sept. 2011), pp. 7494–7502. DOI: 10.1021/nn2024539.

[64] Yu-Jun Zhai et al. “Improved mechanical properties of epoxy reinforced by low content nanodiamond powder”. In: *Materials Science and Engineering: A* 528.24 (2011), pp. 7295–7300. DOI: https://doi.org/10.1016/j.msea.2011.06.053.